

INFORMATION TO USERS

This manuscript has been reproduced from the microfilm master. UMI films the text directly from the original or copy submitted. Thus, some thesis and dissertation copies are in typewriter face, while others may be from any type of computer printer.

The quality of this reproduction is dependent upon the quality of the copy submitted. Broken or indistinct print, colored or poor quality illustrations and photographs, print bleedthrough, substandard margins, and improper alignment can adversely affect reproduction.

In the unlikely event that the author did not send UMI a complete manuscript and there are missing pages, these will be noted. Also, if unauthorized copyright material had to be removed, a note will indicate the deletion.

Oversize materials (e.g., maps, drawings, charts) are reproduced by sectioning the original, beginning at the upper left-hand corner and continuing from left to right in equal sections with small overlaps. Each original is also photographed in one exposure and is included in reduced form at the back of the book.

Photographs included in the original manuscript have been reproduced xerographically in this copy. Higher quality 6" x 9" black and white photographic prints are available for any photographs or illustrations appearing in this copy for an additional charge. Contact UMI directly to order.



University Microfilms International
A Bell & Howell Information Company
300 North Zeeb Road, Ann Arbor, MI 48106-1346 USA
313/761-4700 800/521-0600

Order Number 9234432

Clusters as models of bulk surfaces and novel materials

Jin, Changming, Ph.D.

Rice University, 1992

U·M·I

300 N. Zeeb Rd.
Ann Arbor, MI 48106

RICE UNIVERSITY

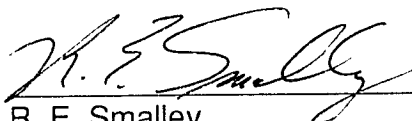
CLUSTERS AS MODELS OF BULK SURFACES AND NOVEL MATERIALS

BY
CHANGMING JIN

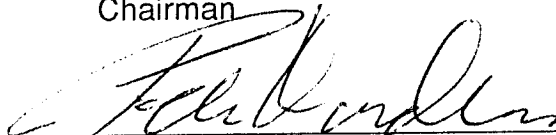
A THESIS SUBMITTED
IN PARTIAL FULFILLMENT OF THE
REQUIREMENTS FOR THE DEGREE

DOCTOR OF PHILOSOPHY

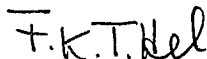
APPROVED, THESIS COMMITTEE:



R. E. Smalley
Professor of Physics and Chemistry
Chairman



P. J. A. Nordlander
Assistant Professor of Physics



F. K. Tittel
Professor of Electrical and Computer
Engineering

Houston, Texas

April, 1992

ABSTRACT

Clusters as Models of Bulk Surfaces and Novel Materials

by

Changming Jin

Studies on gas phase clusters show that common ground exists between clusters and bulk surfaces such that clusters can serve as models of bulk surfaces. Several cluster systems are studied to probe this cluster-surface analogy with both ultraviolet photoelectron spectroscopy (UPS) and Fourier transform ion cyclotron resonance (FT-ICR). Ultraviolet photoelectron spectra of GaAs cluster anions are measured with a photon energy of 7.9 eV. The electron affinity displays a strong even/odd oscillation suggesting the presence of a substantial gap between the highest occupied molecular orbital (HOMO) and the lowest unoccupied molecular orbital (LUMO) in the corresponding neutral clusters. The absence of unpaired electrons in even numbered neutral clusters is reminiscent of the healed dangling bonds caused by the reconstruction and relaxation at GaAs bulk surfaces.

Chemical reactions of noble and transition metal clusters with CO and H₂ are studied with FT-ICR. The chemistry and physics of these metal cluster plus adsorbates systems are also modeled well by using the cluster shell model originally developed for metal bulk solids and surfaces. Excellent interplay between theory and experiment on the Cu_x+CO systems reveals the major advantage for the cluster model of bulk surfaces.

New materials are prepared in the course of studying gas phase carbon clusters. Laser vaporization of a graphite/BN composite disk produces fullerenes in which one or more atoms of the hollow carbon cage is replaced by a boron atom. These boron-doped fullerenes are found to act as Lewis acid when they chemisorb ammonia molecules. Fullerenes with one or more metal atoms inside are also generated both in gas phase and in macroscopic quantities. The formation mechanism of the multi-metal doped fullerenes is proposed as due to coalescence. These new materials are expected to have interesting, novel, and useful properties.

ACKNOWLEDGEMENTS

I would like to thank my advisor Professor Smalley for the opportunity to work in one of the world's leading laboratories in the field of cluster science and for his advice and encouragement. I also thank Professor Nordlander and Professor Tittel for serving on my thesis committee.

Josie Conceicao and Dr. Kelly Taylor provided assistance on the GaAs project. They and Dr. Lai-Sheng Wang worked with me on several other UPS experiments. Kelly and Lai-Sheng also proofread my thesis. I appreciate their help as well as the time we have spent together.

Ting Guo deserved a lot of credit in nearly all of the ICR work described here. Dr. Tapani Laaksonen participated in the Cu_x^+CO project and Dr. Lihong Wang updated the computer system. I thank them for their invaluable contributions to this thesis.

I wish to thank Dr. Mike Alford, Yan Chai, Felipe Chibante, Robert Haufler for the collaboration in the metallofullerene work.

Ms. Jo Ann Tammins must be acknowledged for her kindness and happy personality.

Finally I am indebted to my parents for their love, patience and belief.

TABLE OF CONTENTS

Abstract		ii
Acknowledgements		iv
Table of Contents		v
List of Tables		vii
List of Figures		viii
Chapter One	Introduction	1
Chapter Two	UPS of GaAs Clusters	4
2.1	Healing of Dangling Bonds at Bulk Surfaces	4
2.2	Dangling Bonds of Ga _x As _y Clusters	6
2.3	UPS Experimental	7
2.4	Results and Discussion	17
Chapter Three	Shell Closing in Metal Cluster Plus Adsorbate Systems	32
3.1	Jellium Model of Metal Surfaces	32
3.2	Cluster Analog of the Surface Jellium Model	
	----- Cluster Shell Model	33
3.3	Metal Cluster Plus Adsorbate Systems	35
3.4	FT-ICR Experimental	40
3.5	Results and Discussion	51
	3.5.1 Noble Metal Clusters	51
	3.5.2 Transition Metal Clusters	58
Chapter Four	Doped Fullerenes	62
4.1	Fullerenes and Their Derivatives	62
4.2	Cage-doped Fullerenes with Boron	65

4.3	Metallofullerenes	74
Chapter Five	Conclusions and Outlook	81
References		84

LIST OF TABLES

Table I	Electron affinity of Ga_xAs_y clusters	25
Table II	Chemisorption energy of CO on copper clusters	37
Table III	Calculated LUMO energy of Cu_x^+ clusters	39

LIST OF FIGURES

Figure 1	Edge view of GaAs(110) surface	5
Figure 2	UPS cluster source and TOF mass spectrometer	8
Figure 3	Cross section of the photoelectron spectrometer	9
Figure 4	Laser vaporization source	10
Figure 5	Expanded view of the photodetachment region	14
Figure 6	UPS of Ga_xAs_y^- clusters in the 2-11 atom size range	18
Figure 7	UPS of Ga_xAs_y^- clusters in the 12-21 atom size range	19
Figure 8	UPS of Ga_xAs_y^- clusters in the 22-31 atom size range	20
Figure 9	UPS of Ga_xAs_y^- clusters in the 32-41 atom size range	21
Figure 10	UPS of Ga_xAs_y^- clusters in the 42-50 atom size range	22
Figure 11	Electron affinity of Ga_xAs_y clusters	24
Figure 12	TOF mass spectrum of Ga_xAs_y^- clusters	26
Figure 13	UPS of As_2^-	28
Figure 14	UPS of 23 atom Ga_xAs_y^- clusters	30
Figure 15	FT-ICR apparatus	41
Figure 16	FT-ICR cluster source	42
Figure 17	Cross section of the ICR cell	44
Figure 18	CID of $\text{Cu}_x^+ + \text{CO}$ clusters ($x=6-12$)	52
Figure 19	Relative reactivity of Cu_x^+ with CO ($x=6-12$)	53
Figure 20	CID of $\text{Cu}_x^+ + \text{CO}$ clusters ($x=15-21$)	56
Figure 21	CID of $\text{Au}_x^+ + \text{CO}$ clusters ($x=5-9$)	57
Figure 22	Relative reactivity of cobalt clusters with H_2	60
Figure 23	FT-ICR mass spectra of C_n and B_mC_{n-m} clusters	67
Figure 24	Expanded view of the mass spectra of 60 atom clusters	68

Figure 25	Ammonia titration of boron doped C ₆₀	71
Figure 26	Photolysis of boron doped C ₆₀	73
Figure 27	Expanded view of the mass spectrum around 860 amu	75
Figure 28	FT-ICR mass spectrum of metallofullerenes	76
Figure 29	FT-ICR LDMS of La@C _n a containing film	79
Figure 30	FT-ICR LDMS of toluene extracted La@C _n materials	78

Chapter One

Introduction

Clusters are aggregates of atoms anywhere between two to tens of thousands. Interest in the physics and chemistry of these clusters has grown considerably in recent decades [1], partially driven by the desire to use clusters as models of bulk surfaces [2,3] and novel materials [4].

In the field of surface science, most of the experiments are done on macroscopic single crystal surfaces which are idealized models of real polycrystalline surfaces of practical importance. There is clearly a lack of symmetry normal to the surface, and in some cases, e.g. partial chemisorption on surfaces, little or no symmetry can be found at a specific surface site. For theoreticians it is very difficult to handle the infinite number of atoms without extensive symmetry. Drastic simplifications have to be made to model the real experimental situation ----- consider only a few layer slab or just a few atoms in the form of a small cluster to mimic the presumed active site under study on the real surfaces. Due to this relatively weak coupling between experiment and theory, most of experimental publications are descriptive in nature, and most theories are only intended to be suggestive.

For a small cluster, a large portion of its atoms are located on the surface, and it would in many aspects act like and serve as a model of a bulk surface. The principle advantage of such a "cluster model" would be that it is small

enough to be an easier target for fundamental first-principle theoretical calculations. With the rapid development of laser vaporization and cluster beam technology [5-7], clusters can be produced with virtually any material that can be fabricated into an appropriate target. Clusters of semiconductors, transition metals, and main group metals have all been made this way. These clusters then can be mass selected and annealed to a single geometric structure, and their physical and chemical properties can be studied in the gas phase under ultrahigh vacuum (UHV) environment, much like in a typical bulk surface science experiment but with intimate coupling to theoretical calculations. In some aspects, gas phase cluster techniques provide an alternative way to understand the physics and chemistry of real bulk surfaces from a microscopic point of view. Furthermore, the states of clusters (mass, charge, *etc.*) can be systematically varied in small increments so that one can readily test if an agreement between theory and experiment is fortuitous.

On the other hand, cluster science is a relatively young field compared to that of the bulk solids and surfaces. Since clusters lie between atoms or molecules and bulk surfaces, the approaches and models of studying them have come from both sides. Models developed for bulk surfaces have also been applied to clusters.

The first part of this thesis describes studies of common ground between clusters and bulk surfaces in terms of models and phenomena. All the clusters in this work are generated by laser vaporization followed by supersonic expansion and studied in gas phase. In the next chapter, we will show the ultraviolet photoelectron spectra (UPS) of Ga_xAs_y cluster anions obtained on the UPS apparatus, and present our analysis of the data and the relationship

between the clusters and bulk surfaces in term of the healing of the dangling bonds. In chapter 3, we will apply the cluster shell model, which is originated from the jellium model developed for metal bulk surfaces, to cases of metal cluster plus adsorbate systems and chemical reactions of transition metal clusters with H_2 . As an example of the good interplay between theory and cluster science experiment, we will compare the results of the Cu_x+CO experiment with those of high level theoretical calculations.

Although there are similarities between clusters and real bulk surfaces, the physical properties of the small clusters generally differ from those of the bulk solids, as well as from the properties of free atoms or molecules. Clusters of a certain size and synthesized with proper ways may offer opportunities for new materials with novel properties. Desire to produce materials such as nanosized catalysts, nanowires, and quantum crystals, *etc.* have stimulated increasing interest in this new area.

In 1985, a new cluster molecule C_{60} was discovered at Rice University during the course of studying supersonic carbon cluster beams [8]. This discovery together with the ability to produce macroscopic quantities of this cluster molecule developed later on [9,10] have amazed the whole scientific community [11]. A new class of cluster molecules called fullerenes has emerged. In chapter 4, we will describe the doping of these fullerene clusters, hoping that these doped cluster molecules will find their use in the future as novel materials.

Chapter Two

UPS of GaAs Clusters

2.1 Healing of Dangling Bonds at Bulk Surfaces

GaAs, because of its technical importance, is one of the most widely studied semiconductor materials [12]. It serves as a prototype of a weakly ionic semiconductor. In the bulk form it is a direct band gap semiconductor with a band gap of about 1.5 eV [13], and crystallizes into the zincblende structure where cations and anions are arranged alternatively on a diamond lattice. An infinite two-dimensional plane that slices through and breaks a periodic array of the GaAs tight-bonding hybrid orbitals forms an ideal surface. When the surface bonds are broken, hybrid bonding and anti-bonding states revert to the original single atom hybrid energy position, and this "surface-localized" level lies in the fundamental gap to form a surface state. The ideal surfaces are usually unstable and reconstruct and relax themselves to form more stable atomic arrangements. Cleavage of the surface along the GaAs(110) plane, for example, results in a surface with gallium or arsenic atoms each having a single sp^3 dangling bond. In the absence of reconstruction this would leave a metallic surface density of states. However, reconstruction does occur by the outward motion of the arsenic atoms and the inward motion of the gallium atoms (see Figure 1), leaving the surface gallium atoms with an unoccupied dangling bond, and the surface arsenic atoms with a dangling lone-pair [14]. Such surface reorganizations effectively sweep the dangling bond states out of the gap in the

surface density of states, producing a semiconducting surface [15-17]. Similarly effective relaxations or reconstructions are thought to occur on the other low miller indices surfaces of GaAs.

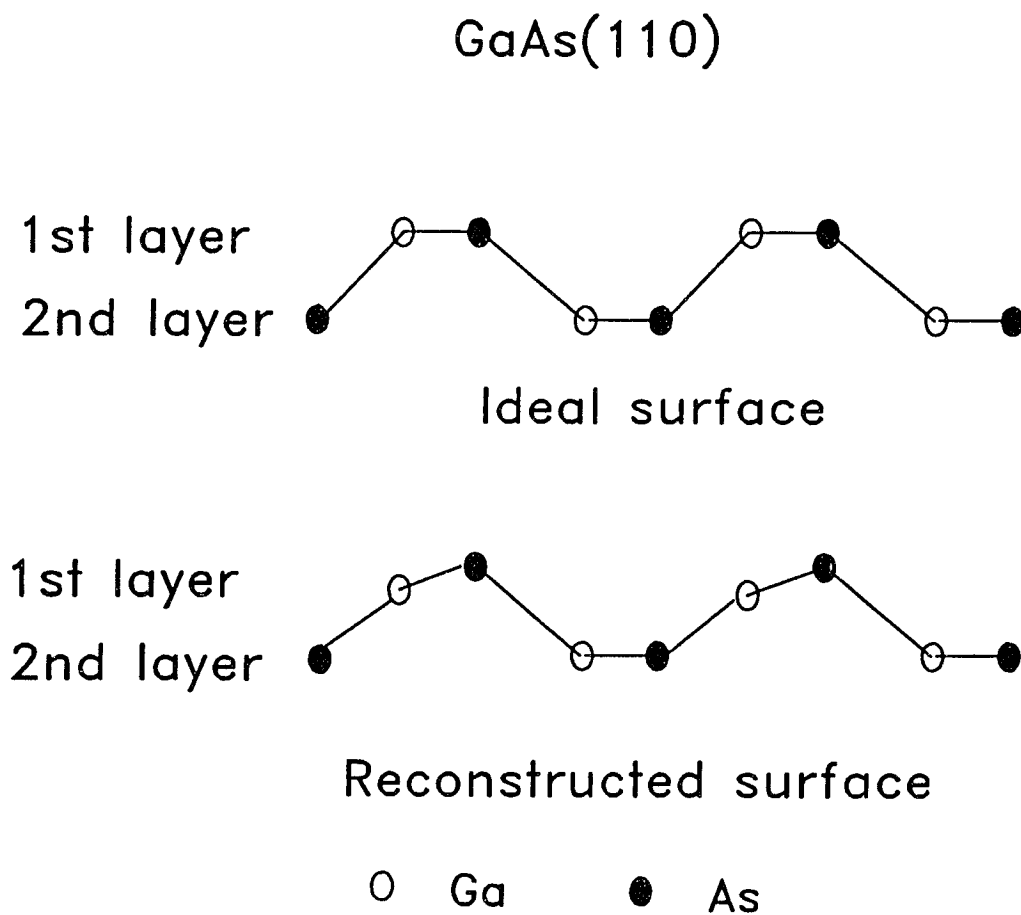


Figure 1. Edge view of the ideal surface and the reconstructed surface of GaAs(110).

2.2 Dangling Bonds of Ga_xAs_y Clusters

For small gallium arsenide clusters, most of the atoms are surface atoms, and with the ideal sp^3 hybridized configuration, there would be dangling bonds associated with these surface atoms just like in the case of ideal bulk surfaces. It is important to establish how effective surface reconstruction can be in healing the dangling bonds of these small clusters.

Nearly five years ago in an initial supersonic cluster beam experiment with gallium arsenide clusters, O'Brien *et al.* discovered a remarkable even/odd alternation in the ionization potentials (IP) [18]. Since the clusters were prepared by laser vaporization of a gallium arsenide disk in a high pressure pulsed supersonic nozzle, the clusters formed in a highly supersaturated vapor of gallium and arsenic atoms, and a wide range of Ga_xAs_y compositions were generated for every cluster size, $n = x+y$. Even so the remarkable observation was made that all even numbered clusters in the size range from 4 to 22 atoms had IPs higher than 6.4 eV, while the odd numbered clusters with 5-21 atoms all had ionization thresholds less than 6.4 eV. Somewhat later Liu *et al.* [19] reported results from a bracketing of the thresholds for photodetachment of electrons from the negative cluster ions of Ga_xAs_y in the 2-30 atom size range, thereby providing rough estimates of the vertical electron affinity (EA). Again even/odd alternation appeared, with the odd numbered clusters having the larger EA values.

The supersonic beam source used in this experiment produced clusters with a wide range of compositions, making the question of surface reconstruction to appear at first to be impossibly complex. Yet the strong even/odd alternation

in IP and EA for these clusters suggested that this reconstruction might be highly efficient. If so, it is possible that the even/odd alternation in IP and EA will continue through very large clusters, extrapolating to the bulk band gap. The ultraviolet photoelectron spectra (UPS) survey experiments presented below are designed to test this hypothesis and to provide information on the dangling bonds on these cluster surfaces.

2.3 UPS Experimental

The detailed description of the UPS apparatus has been given elsewhere [20]. It consists of a cluster source, a time of flight mass spectrometer (TOFMS), and a photoelectron spectrometer. Figure 2 shows the cluster source and the TOF mass spectrometer, and Figure 3 displays the horizontal cross section of the photoelectron spectrometer.

Clusters are generated by means of laser vaporization followed by supersonic expansion. This method was pioneered by Smalley and coworkers [5], and is now widely used as one of the standard techniques in the cluster field. A cross section of the laser vaporization source used on the UPS apparatus is shown in Figure 4. It involves the use of two fast pulsed valves of the magnetic "current loop" variety [21] (a commercial version derived from this pulsed valve design is available from R. M. Jordon Company, Grass Valley, CA) bolted to opposite sides of a 1.5 cm wide Teflon nozzle block. The opposing gas flow from these two valves (pulse duration 125 ms, $0.12 \text{ cm}^3 \text{ atm}$ flow per pulse) is synchronized to meet in a cylindrical "waiting room", 0.3 cm diameter, 1.0 cm long drilled in to the center of the nozzle block.

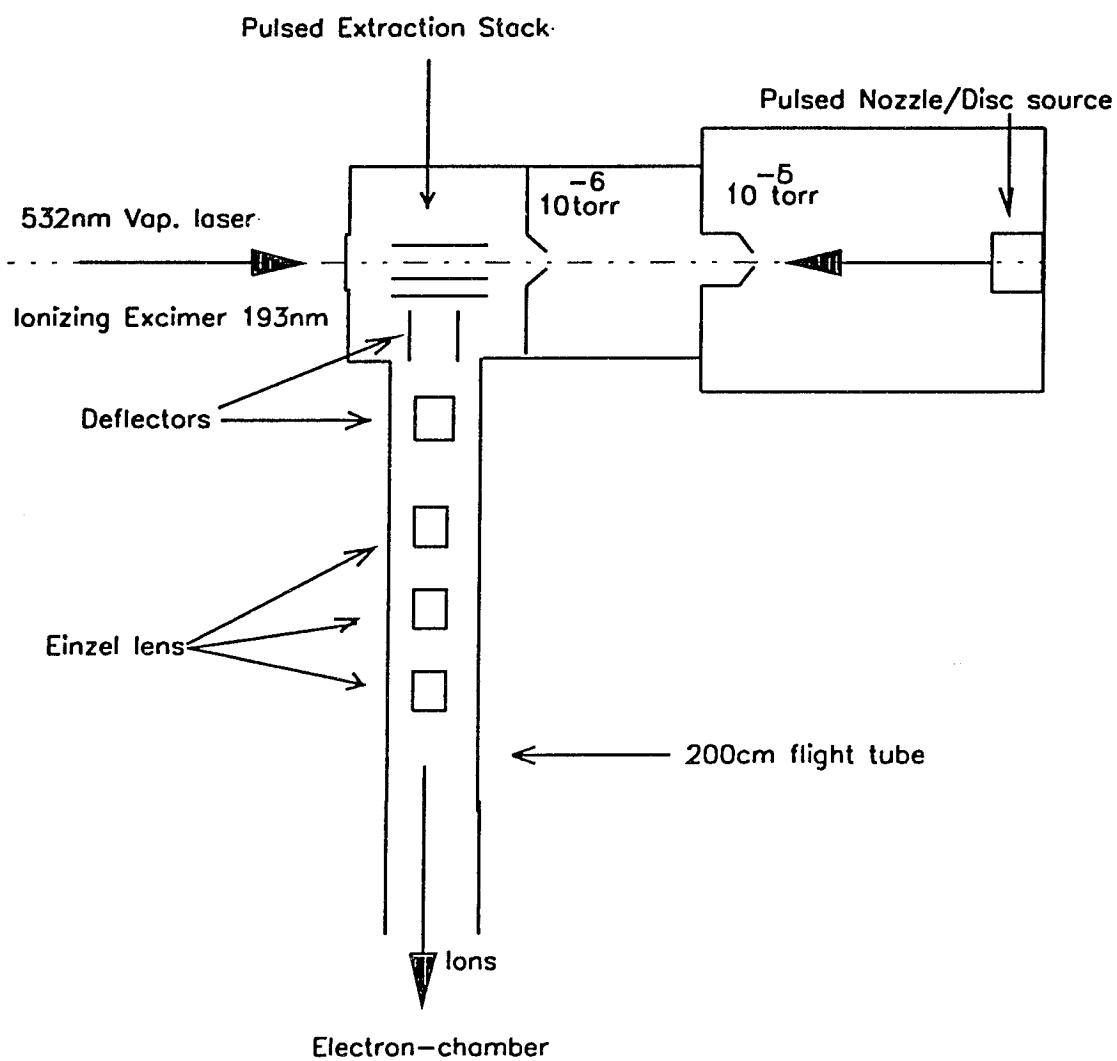


Figure 2. Cross section of the UPS cluster source and the TOF mass spectrometer [22].

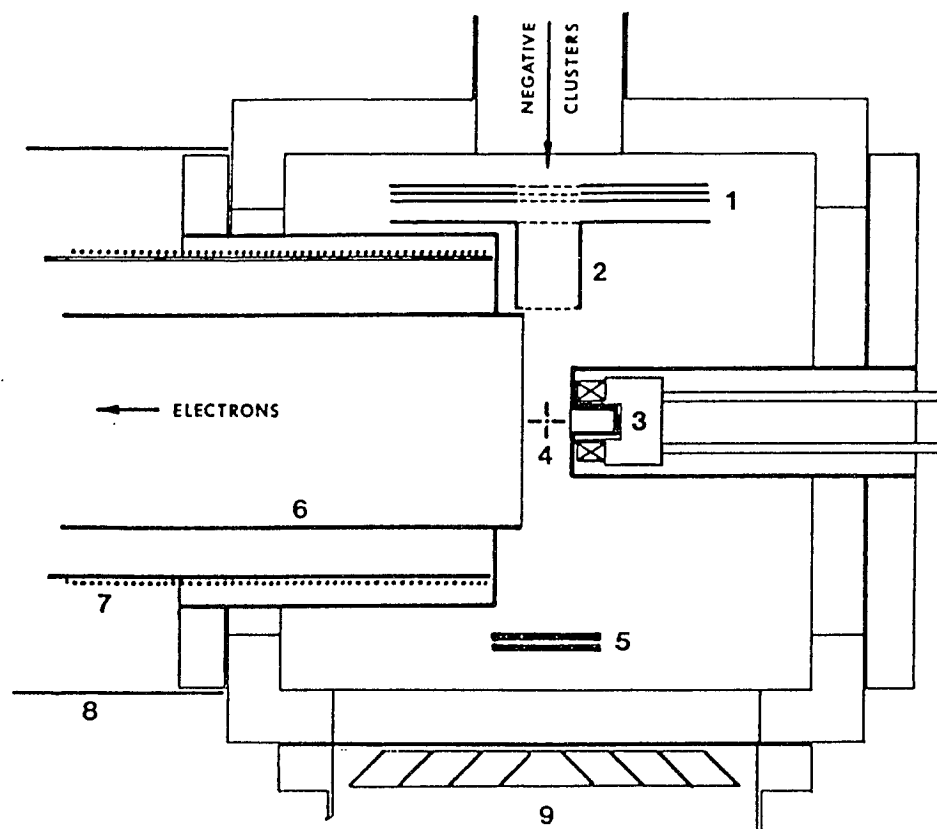


Figure 3. Horizontal cross section of the photoelectron spectrometer. 1. Pulsed mass gate. 2. Pulsed decelerator. 3. Water-cooled pulsed solenoid. 4. Laser interaction zone. 5. In-line dual microchannel plate ion detector. 6. Photoelectron flight tube. 7. Low field guiding solenoids. 8. mu metal shielding. 9. Cryogenic pump. [20]

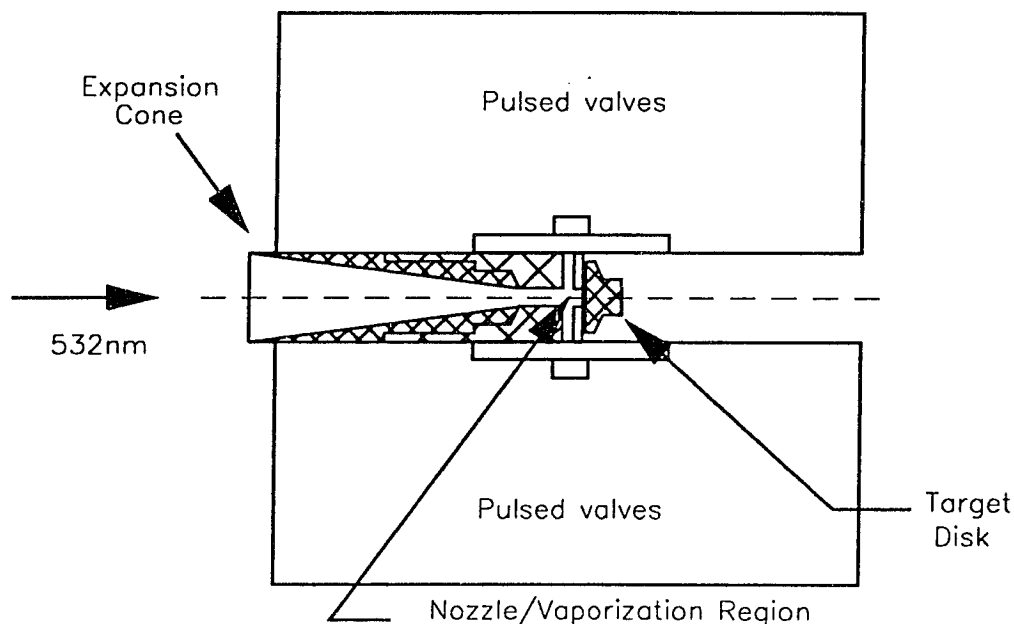


Figure 4. Cross section of the UPS laser vaporization source [22].

The target disk is an undoped GaAs wafer, 0.1 cm thick and 1.2 cm in diameter, glued on to an aluminum mount. The seal to the nozzle block is provided by a Teflon o-ring that slides over the outside of the target disk. The position of the disk is controlled by two motors, one for rotation and the other for vertical displacement. One of the critical parameters involved to obtain good reliable cluster intensities is the alignment of the vaporization laser through the nozzle block. There is a window mounted on the flange behind the nozzle central axis. When desired, the disk is moved downward to clear the central axis so that the laser light can travel through the skimmer, the central axis of the nozzle and the exit window. Good alignment is achieved by monitoring the shape of transmitted laser spot.

We use the second harmonic of a Nd-YAG laser (5-ns pulse length, 10-30 mJ/pulse) as our vaporization laser and helium (Linde, research grade 99.995% purity) as the carrier gas. After the two fast valves are opened, He gas starts to flow into the nozzle and the pressure in the nozzle increases. On the rising edge of this He pressure build up, the vaporization laser is fired which travels down the axis of the supersonic beam apparatus through the cylindrical waiting room, and focused to a 0.1 cm diameter spot on the GaAs target disk and vaporize the material to form a hot plasma. The GaAs plasma is cooled and condensed to form clusters by the He buffer gas in the waiting room. The clusters (of all positive, neutral and negative charge states) are then seeded in the He gas and accelerated through a 0.2 cm diameter orifice, and expand through a 6 cm long 10° internal angle nozzle cone.

The He pressure inside the nozzle before expansion is estimated around $P_0 = 200$ Torr [23], which gives a mean free path of $\lambda_0 = 10 \times 10^{-4}$ cm. Since the orifice diameter D_0 (0.2 cm) is much larger than λ_0 ($D_0 \gg \lambda_0$), there will be many collisions as the gas flows through the orifice and downstream in the expansion cone. This will convert the enthalpy associated with random atomic motion into directed mass flow, and therefore cause the mass flow speed, u , to increase and the translational temperature T to decrease. The Mach number, M , is defined as

$$M = u / a \quad (1)$$

where $a = (\gamma kT/m)^{1/2}$ is the local speed of sound and γ is the specific heat ratio. When M is greater than one, the expansion is termed as supersonic expansion. Given the temperature in the nozzle T_0 , the translational temperature in the beam can be expressed as

$$T = T_0 / [1 + (\gamma - 1)M^2/2] \quad (2)$$

The rotational and translational temperature of the clusters are substantially cooled down through collisions during the supersonic expansion process. The vibrational temperature, however, due to the relatively larger gaps between vibrational energy levels, is not cooled as much. Nevertheless the overall cluster temperature after the supersonic expansion is estimated to be equal or below room temperature in this experiment.

After the supersonic expansion, the cluster beam goes through a skimmer, which serves both for collimation and differential pumping. The clusters then enter a Wiley-McLaren [24] type pulsed extraction stack located in the center of the ion extraction chamber. The stack is tilted [25] operating at 1000 volts.

The time of flight mass spectrometer axis is perpendicular to the cluster beam axis. The cluster anions have the same kinetic energy along the TOFMS axis as they exit from the extraction stack ---- cluster anions with different mass will have different velocity and arrive in the photoelectron detachment region at different time. Thus we can measure photoelectron spectra of mass selected cluster anions based on their arrival time.

As shown in Figure 3, the photoelectron spectrometer has four main parts: a mass gate, a deceleration tube, a magnetic solenoid, and an electron time-of-flight tube.

The mass gate consists of three parallel metal plates with central holes. Two outer plates are at ground potential. The central plate is kept at -1100 V to prevent cluster anions from coming through. When the negatively charged clusters with desired mass arrive at the mass gate, the central plate is pulsed to

ground potential to let the anions go through, then it is brought back to -1100 V again.

The most crucial limitation on the resolution in the photoelectron spectrometer stems from the finite velocity of the cluster anions [20]. To increase the energy resolution, the mass selected cluster anions are slowed down when they enter the deceleration tube which is held at a negative potential (about -800 V). When the whole ion packet is inside the tube, the tube is pulsed to ground potential. Since the ions are wholly inside the tube, their motions are unaffected by the sudden change of the tube potential. As they travel out of the tube, the ions enter the photoelectron detachment region without reacceleration.

We also can ground all the grids of the mass gate and the deceleration tube so that all the cluster anions can pass through. A pair of microchannel plates mounted directly in the flight path of these clusters ions are used to monitor the mass distribution while the cluster signals are being optimized.

An expanded view of the photoelectron detachment region is shown in Figure 5. As the cluster anions drift through this region, a detachment laser is fired perpendicular to the cluster beam. Just before the firing of the laser, a strong and divergent magnetic field is produced by a pulsed electromagnet. The peak strength of this magnetic field at the center is 5000 G. Photoelectrons detached in such a strong field are constrained to follow the local field lines. They are guided to drift in an electron time of flight tube by a weak static field produced by a long solenoid magnet mounted coaxially along the full 234-cm length of the flight tube. This magnetic bottle design has an electron collection

efficiency greater than 98% because the magnetic mirror effect ensures that virtually all the photoelectrons are directed to the electron flight tube.

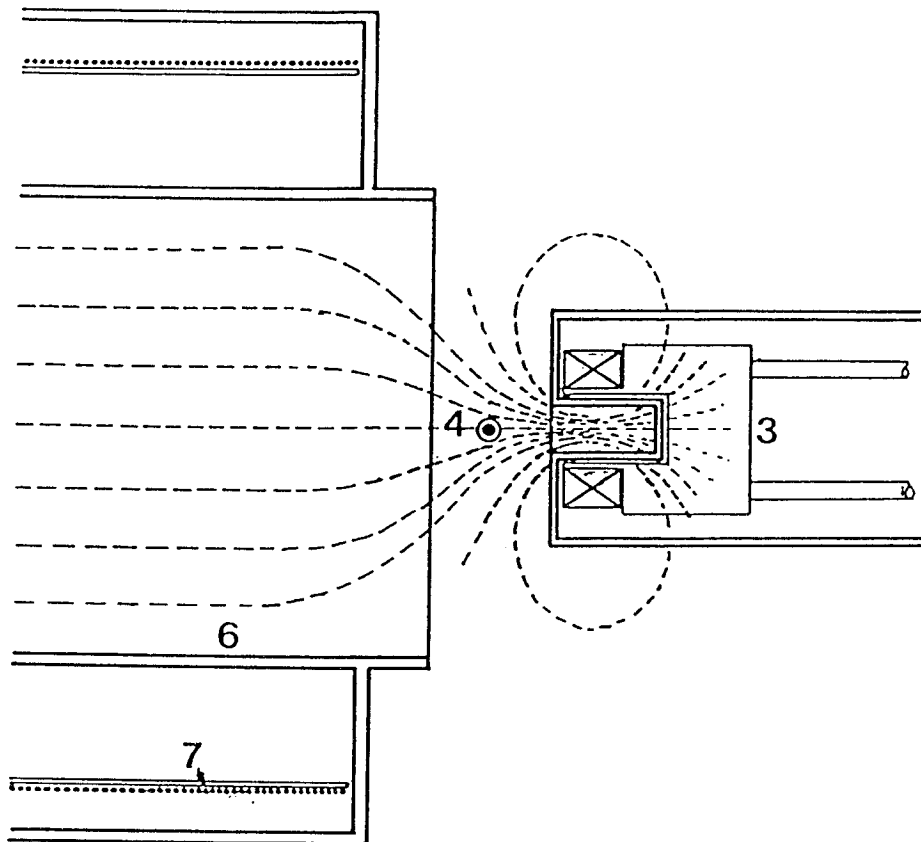


Figure 5. An expanded view of the photodetachment region. See Figure 3 for the labels.

In UPS experiments, one of the key problems is the background photoelectron noise. With intense detachment laser and high photoelectron collection efficiencies, extraordinary measures must be taken to avoid the experiment being totally swamped by stray photoelectron signal. In our photoelectron spectrometer, the magnetic field lines map smoothly from the detector at the end of the flight tube to a small central detachment region, and encounter the only metal surface at the back of the central hole of the solenoid as shown in Figure 5. The bulk of the photoelectrons detached from this metal surface by stray laser light will be reflected by the magnetic field as it converges to the peak 5000 G on the way out of to the detector. Photoelectrons from other areas other than the central detachment region are not seen by the detector because the field lines diverge away from the flight tube. To avoid noises due to background gases, a 20-cm-i.d. cryopump (CTI Cryogenics) is used to maintain the best possible vacuum in the detachment chamber. After bakeout, the chamber typically operates at about 1×10^{-10} Torr. The negative cluster beam input flight tube is differentially pumped by a 130 l/s turbopump and a nitrogen cryotrap, and typically operates at 1×10^{-9} Torr. As a result, the stray electron noise from the background (metal surfaces, residual gases, *etc.*) are dramatically reduced.

Electrons travelling down the flight tube are detected by a set of triply staged microchannel plates. The resultant signal is then amplified and recorded on a transient digitizer. The time zero of the digitizer is set by a trigger from a photodiode monitoring the photodetachment laser. From the arrival time of the electron, t , we can calculate its kinetic energy, KE, according to the relation

$$KE = 1/2 m (L/t)^2 \quad (3)$$

where m is the electron mass, L is the length of the flight tube. The binding energy of the electron in the cluster anion is simply

$$E_b = E_I - KE \quad (4)$$

where E_I is the detachment photon energy. To account for systematic errors, adjustable parameters a , b and c are introduced to obtain the binding energy

$$E_b = E_I - [a + b / (t - c)^2] \quad (5)$$

Determination of these parameters, or energy calibration, is done by measuring a photoelectron spectrum of an atomic anion with known electron affinity and energy intervals between distinct atomic lines. Au^- is used in this experiment [26,27].

The whole experimental process is controlled by a IBM PC 386 computer through a CAMAC interface. The cluster anions are generated at a repetition rate of 10 Hz, and the detachment laser is operated at 20 Hz such that half of the laser shots are fired while there are no cluster anions present at the detachment region. The background photoelectron noise signals are subtracted on these alternative shots.

For the Ga_xAs_y experiment described below, negative clusters ions with less than 20 atoms are decelerated to the energy range of 100-200 eV. Above 20 atoms the velocity effect on the resolution is small enough that deceleration from the original 900 eV energy of the pulse extracted Ga_xAs_y^- beam is unnecessary. The effective resolution of the UPS apparatus for the data reported below is 0.05 to 0.1 eV. All the spectra are recorded as the accumulation of data from about 10^4 pulses of the cluster beam apparatus. The resultant photoelectron spectra are smoothed with a 0.05 eV square window function.

2.4 Results and Discussion

In earlier studies of Ga_xAs_y clusters in this group it was noted that the clusters tended to lose arsenic (probably in the form of As_2 and As_4) when heated [18,19,28]. When the laser vaporization cluster nozzle is operated to yield a substantial number of cluster ions derived from the original laser-induced plasma ionization, much of the cluster growth occurs while the buffer gas temperature is rather high. In the case of GaAs this often produces Ga_xAs_y clusters for which the x:y composition distribution is peaked somewhat to the gallium rich side ($x>y$) [28]. We optimize the operation of the cluster nozzle to minimize this arsenic loss as much as possible. Nevertheless, it is clear from careful calibration of the mass spectra of the Ga_xAs_y^- cluster beams used in this study that the distributions are skewed to the gallium-rich side, the maximum occurring near the composition with $x=y+2$.

Figures 6-10 present the recorded UPS spectra of mass-selected Ga_xAs_y^- clusters in the size range $x+y = 2$ through 50. With the exception of the UPS data for the two atom cluster (which refers to the GaAs^- diatomic), our mass resolution is insufficient to pick out a single x,y composition. For the larger clusters, even with orders of magnitude higher mass resolution it would have been impossible to select purely a single x,y composition from the Ga_xAs_y clusters due to the overlapping mass distributions caused by the ^{69}Ga and ^{71}Ga isotopes of gallium in natural abundance. Instead we time the firing of the photodetachment laser to intersect the section of the cluster time-of-flight spectrum corresponding to the time calculated for the stoichiometric 1:1 composition. For the even numbered clusters we chose the photodetachment time appropriate to the $x=y$ composition of the mass-selected Ga_xAs_y^- clusters,

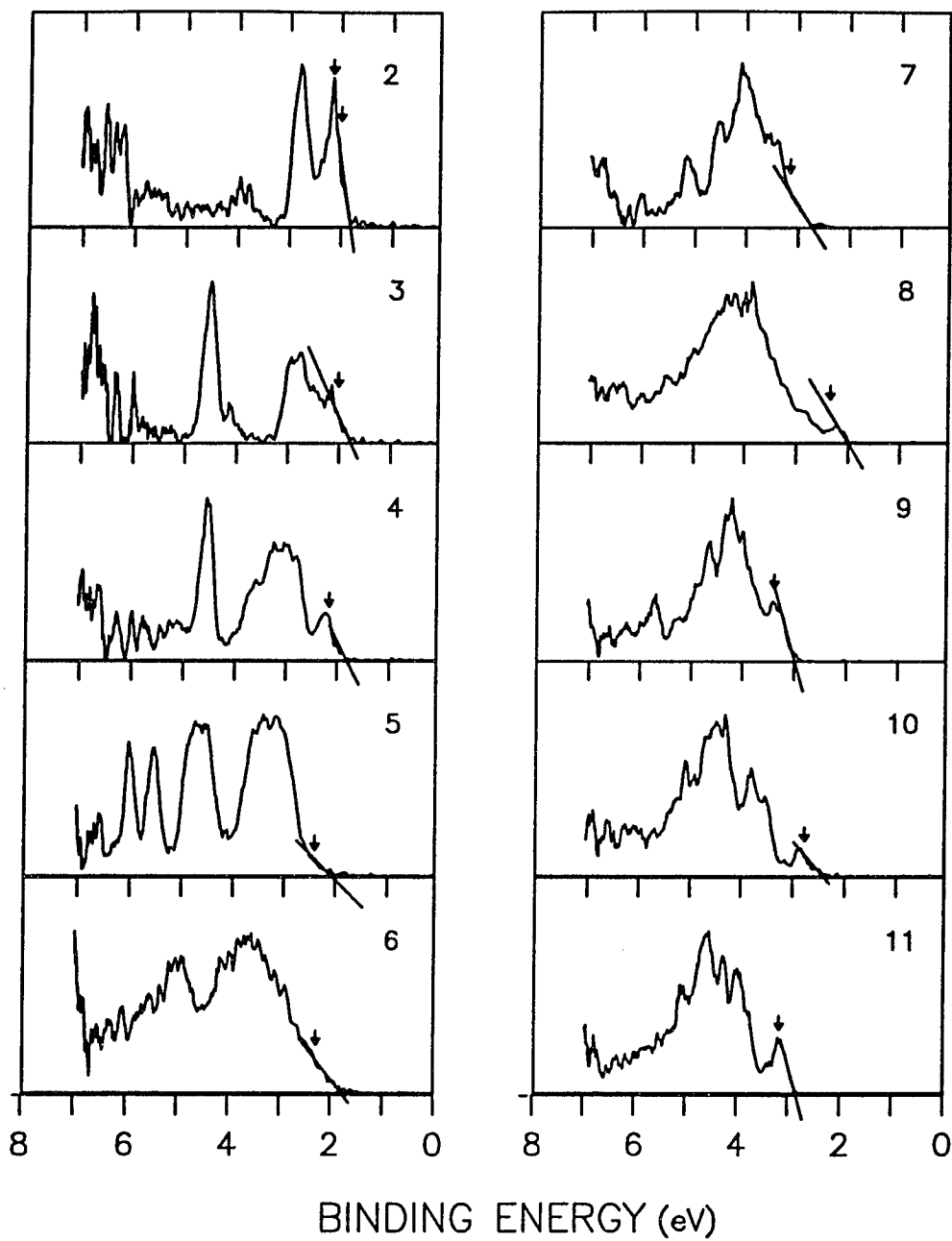


Figure 6. Photoelectron spectra of mass-selected Ga_xAs_y^- clusters in the (2-11) atom size range. The arrows denote the EAs.

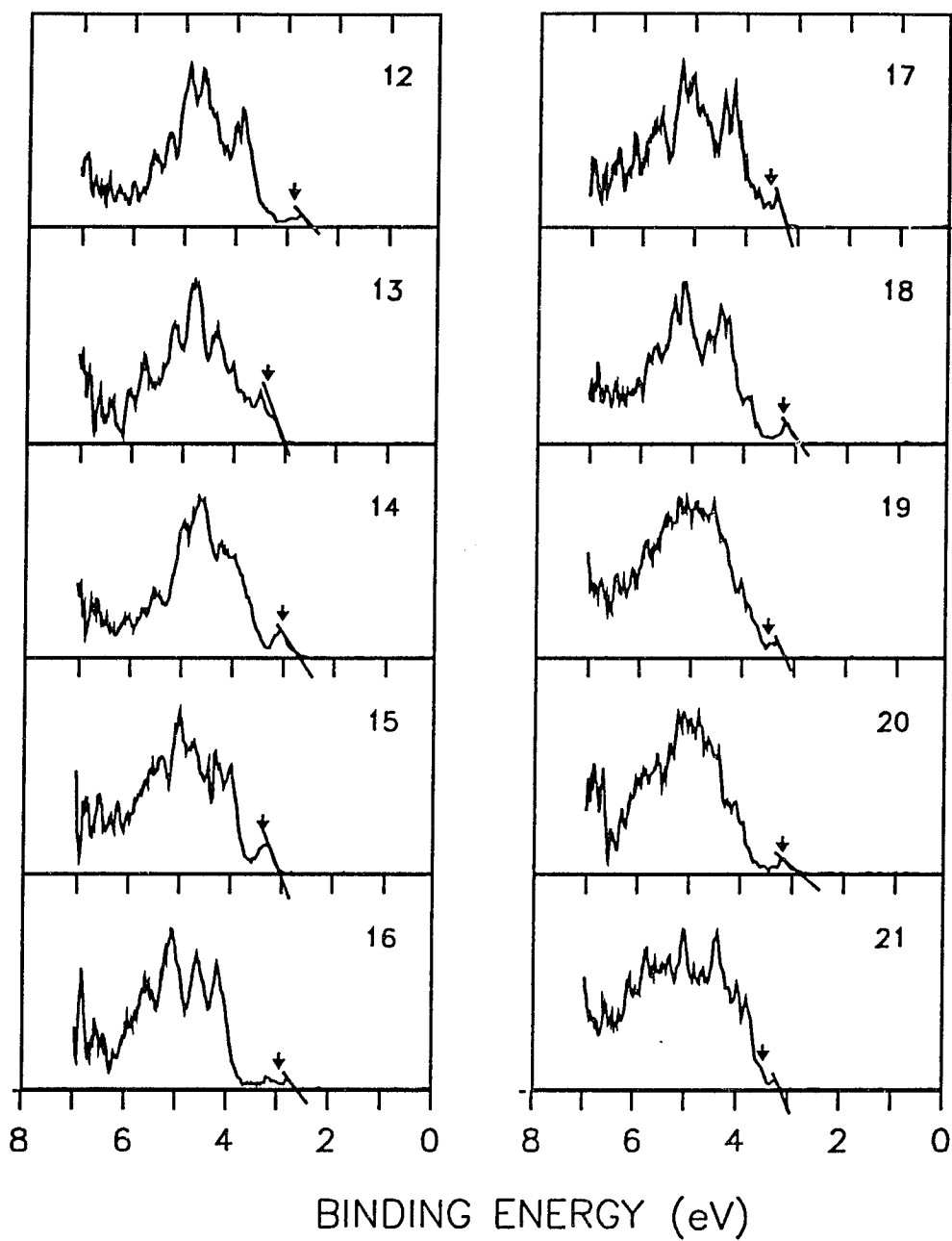


Figure 7. Photoelectron spectra of mass-selected Ga_xAs_y^- clusters in the (12-21) atom size range.

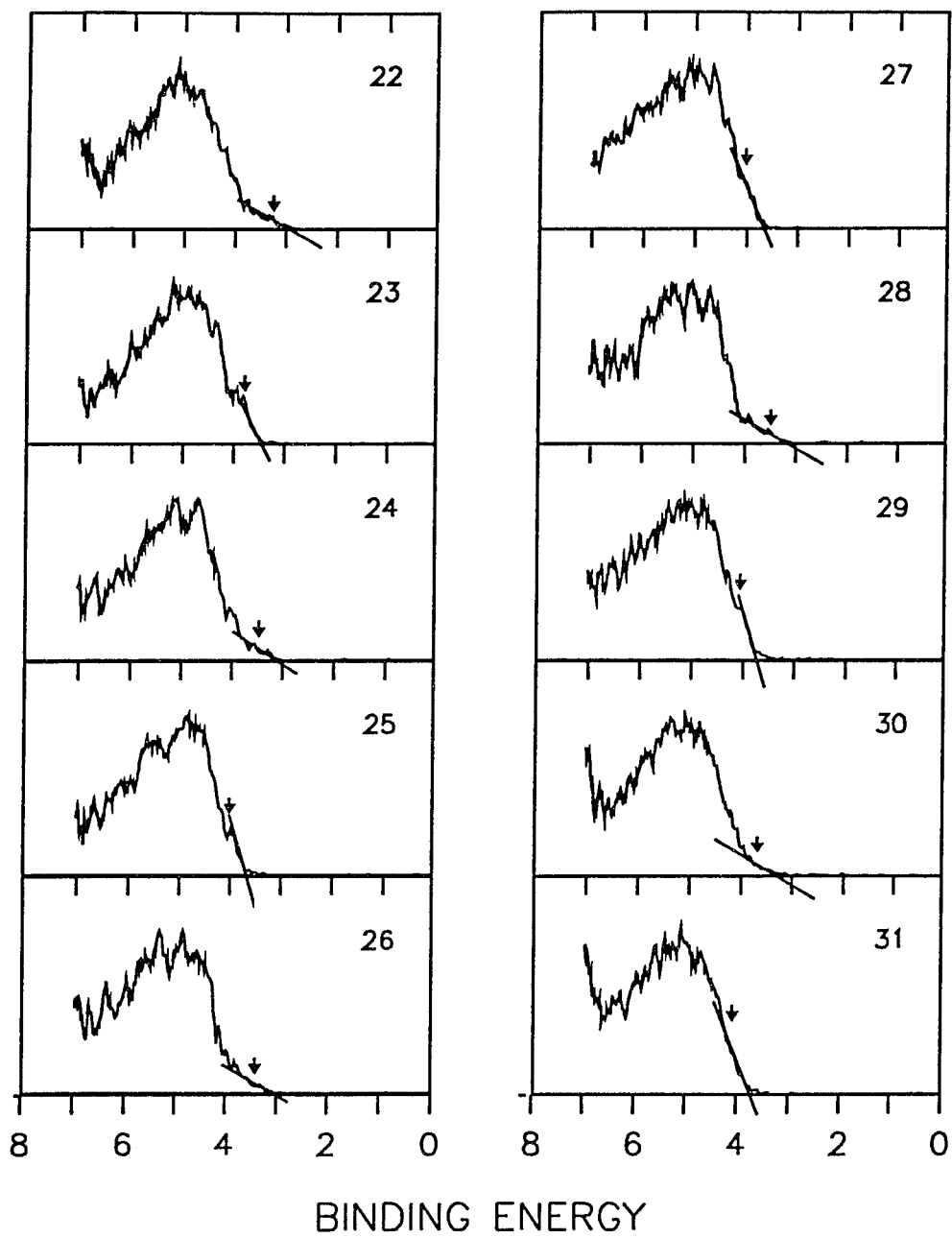


Figure 8. Photoelectron spectra of mass-selected Ga_xAs_y^- clusters in the (22-31) atom size range.

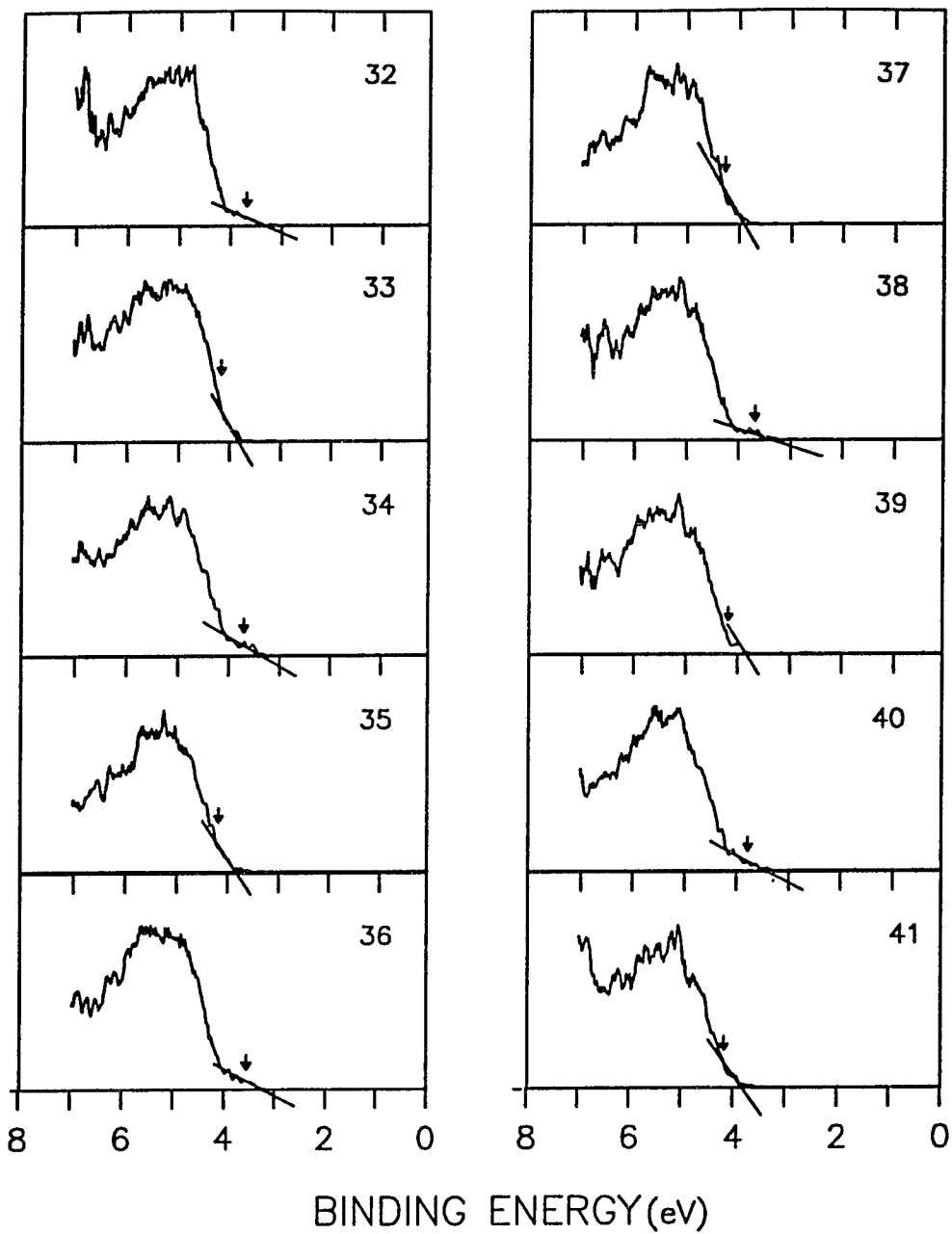


Figure 9. Photoelectron spectra of mass-selected Ga_xAs_y^- clusters in the (22-41) atom size range.

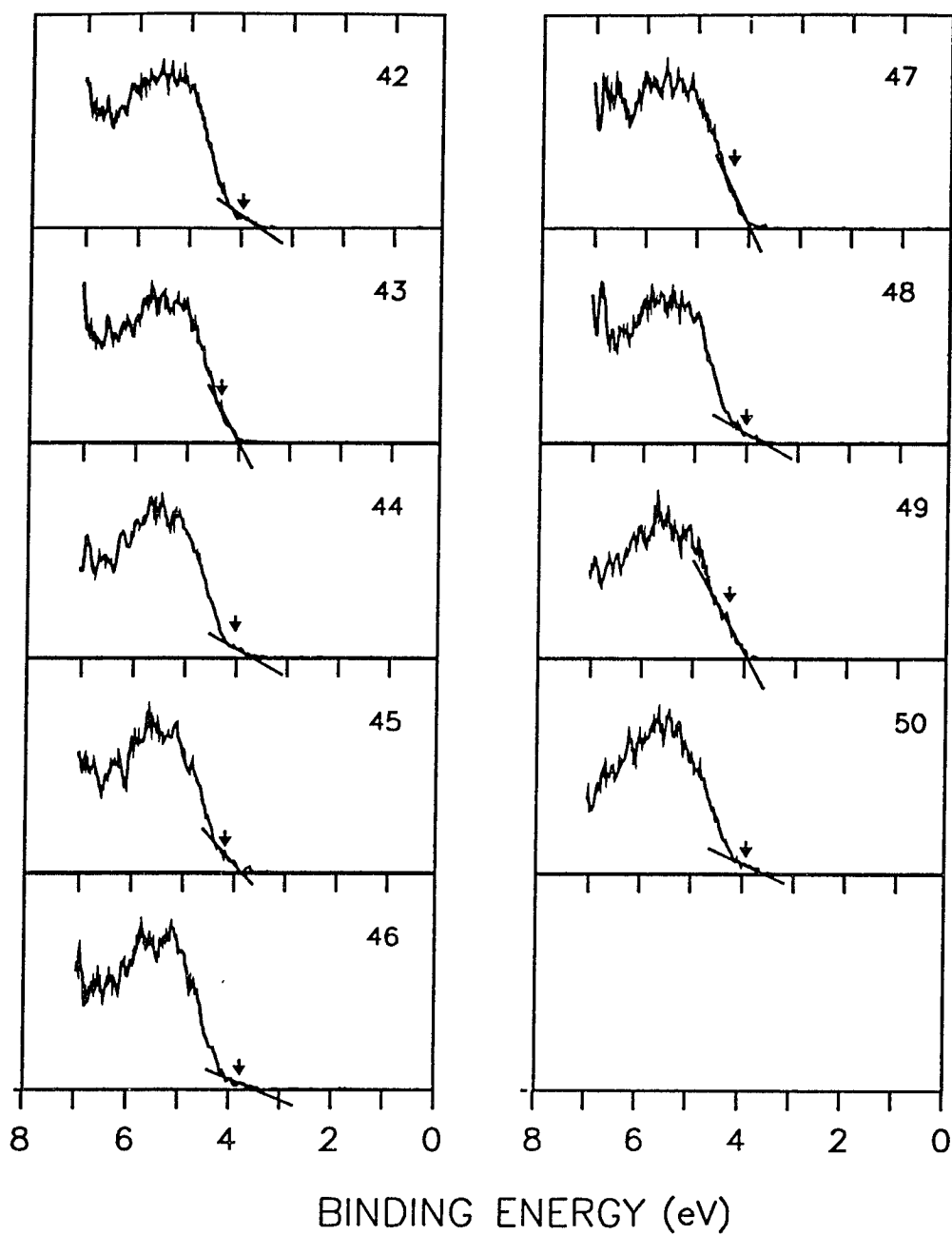


Figure 10. Photoelectron spectra of mass-selected Ga_xAs_y^- clusters in the (42-50) atom size range.

for the odd numbered clusters we chose the time calculated for the $x=y+1$ clusters. It is therefore important in interpreting these spectra to realize that they pertain to a range of cluster compositions, and also most certainly to a range of isomeric structures for each of these compositions as well.

One of the virtues of photoelectron spectroscopy of the negative ions is that the photodetachment threshold provides a direct measure of the vertical electron affinity. In order to estimate the detachment thresholds on such a broad range of poorly resolved spectra we adopt the following simple approach. For each spectrum a straight line fit is made to the rising slope of the first significant spectral feature. The vertical electron affinity is then taken to be the baseline intercept of this straight line plus a constant offset of 0.35 eV as a crude correction for cluster temperature and instrument resolution effects. These EA estimates are tabulated in Table I, and plotted in Figure 11.

As expected from earlier work with GaAs negative clusters [19], even/odd alternation is evident in the EA as a function of cluster size. Although there can certainly be some disagreement with our way of picking the thresholds, we believe any reasonable method will result in the same conclusion: the even/odd alternation in the vertical EA is strong, and this alternation persists without substantial narrowing at least through 50 atoms.

Figure 12 shows a typical Ga_xAs_y cluster anion mass spectrum in the range of 4-18 atoms. It also displays an even/odd alternation in the mass peak height, with the odd numbered cluster anions being more abundant than their even numbered neighbors. This can simply be explained by saying that the odd

numbered cluster anions are more stable because they have higher EA than the even neighbors.

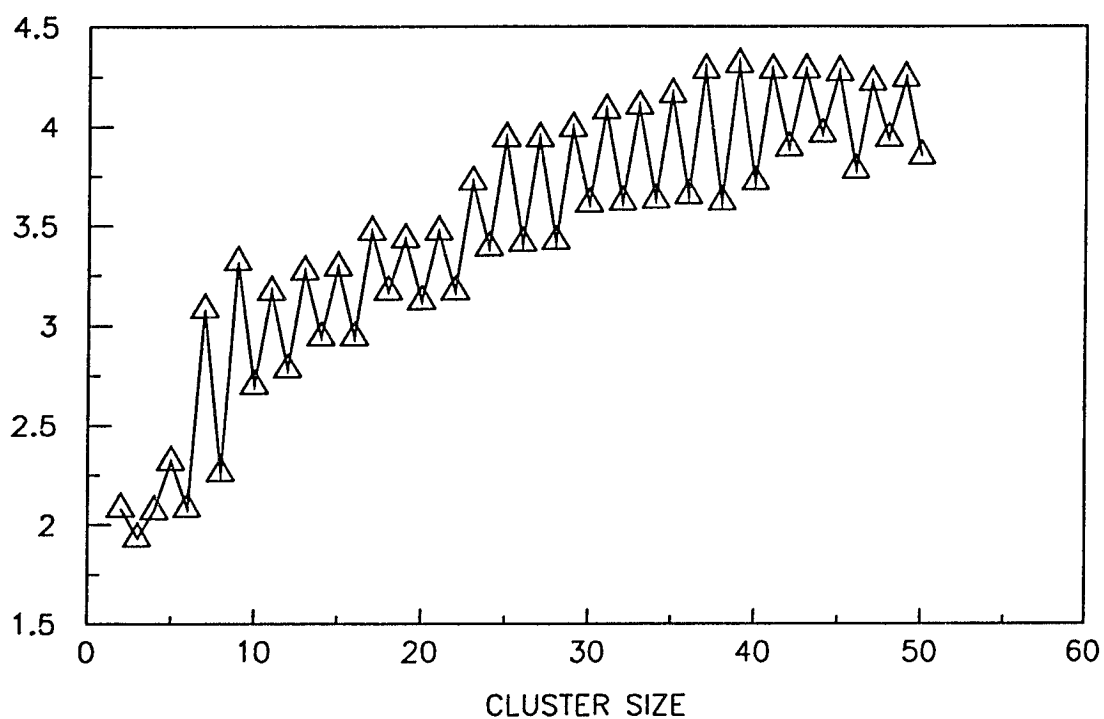


Figure 11. Vertical electron affinity of Ga_xAs_y clusters near the x=y composition as estimated from photoelectron spectra of the mass selected cluster anions.

TABLE I. Estimated vertical electron affinities of Ga_xAs_y^- clusters as a function of cluster size, $n = x+y$.

Cluster size	EA (eV)	Cluster size	EA (eV)	Cluster size	EA (eV)
2	2.1	19	3.4	36	3.7
3	1.9	20	3.1	37	4.3
4	2.1	21	3.5	38	3.6
5	2.3	22	3.2	39	4.3
6	2.1	23	3.8	40	3.7
7	3.1	24	3.4	41	4.3
8	2.3	25	4.0	42	3.9
9	3.3	26	3.4	43	4.3
10	2.7	27	3.9	44	3.9
11	3.2	28	3.4	45	4.3
12	2.8	29	4.0	46	3.8
13	3.3	30	3.6	47	4.2
14	2.9	31	4.1	48	4.0
15	3.3	32	3.6	49	4.2
16	2.9	33	4.1	50	3.9
17	3.5	34	3.6		
18	3.2	35	4.2		

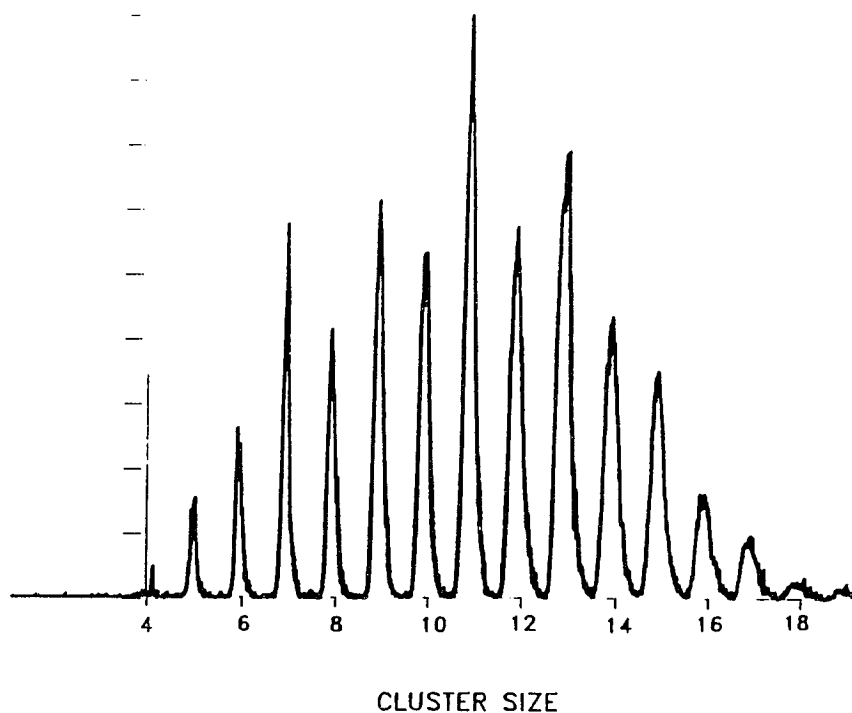


Figure 12. TOF mass spectrum of Ga_xAs_y^- residual ions in the (4-18) atom size range.

The even/odd alternation in IP and EA as a function of cluster size has been a common observation in single-valence-electron metal clusters such as Na[32], K[33], Cu[34], Ag, and Au[35]. In these metal clusters the even/odd alternation arises because the atomic valence orbitals are strongly overlapping and for the small clusters a substantial gap exists between the highest occupied molecular orbital (HOMO) and the lowest unoccupied molecular orbital (LUMO). However, since these elements are all metallic in the bulk phase, it is perhaps not surprising that this HOMO-LUMO gap soon becomes small enough that

even/odd alternation in the IP and EA is no longer observed. In the case of gold clusters the even/odd alternation in IP and EA is extremely pronounced for clusters in the 2-20 atom size range, but it is largely gone by the time the cluster size is greater than 40.

These new EA data of Ga_xAs_y clusters strongly support the notion that relaxation/reconstruction of the surface of these GaAs clusters is highly facile. With the sole exception of the GaAs dimer, all the even-numbered clusters appear to have closed-shell singlet ground states (for the neutral clusters) with substantial HOMO-LUMO gaps. The odd-numbered clusters will of course be open shell species as neutrals simply by virtue of the fact that they have an odd number of electrons, but the observed alternation in the IP of the neutral clusters shows that the HOMO for the odd-numbered clusters is always less tightly bound than for the even-numbered clusters. Results from extended Huckel and local spin density calculations currently underway in this laboratory on gallium arsenide clusters in the 2-20 atom size range are in agreement with this interpretation [28]. The unfilled HOMO of odd-numbered clusters tends to be a largely non-bonding molecular orbital with an energy slightly less than half the HOMO-LUMO gap of the adjacent even-numbered clusters of the same x/y composition. If this trend continues through large clusters, the EA of the even-numbered clusters should asymptotically approach the 4.07 eV electron affinity of the perfect bulk crystal, while the EA of the odd-numbered clusters should evolve to a value slightly below 4.8 eV (the bulk EA plus half the intrinsic band gap).

For the small clusters in the 2-6 atom size range the mass resolution and isotopomer distributions are sufficiently narrow in the experiment to obtain highly

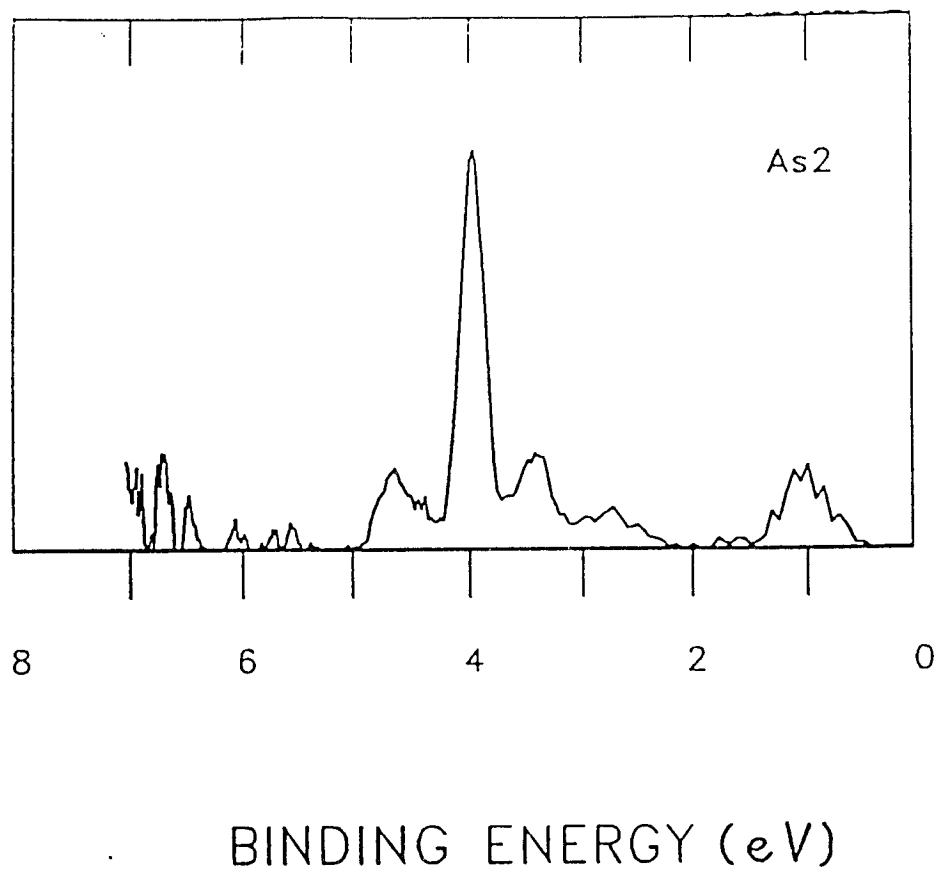


Figure 13. Photoelectron spectrum of As_2^- .

structured UPS patterns for individual compositions. The spectrum shown in Fig. 6 for the diatomic is an example ---- it is from the GaAs^- molecule. In accord with the assignment of the optical spectrum of the neutral molecule [29], and recent theoretical calculations [30,31], this UPS pattern shows that GaAs has an open-shell triplet ground state with an EA which is actually higher than the next odd-numbered cluster. Of all the even-numbered Ga_xAs_y clusters we have

studied, this diatomic is the sole exception to the rule of uniform even/odd alternation in the EA as a function of cluster size. The UPS of another dimer As_2^- is shown in Figure 13. The smaller bump followed by a gap and then several peaks in the spectrum clearly indicate that this diatomic molecule has a closed-shell ground state, in agreement with theoretical calculations [28,30].

The photoelectron spectra plotted in figures 6-10 are for stoichiometric Ga_xAs_y cluster anions. Since arsenic atom is more electronically negative than gallium, it is interesting to see how the EA changes as we change the x/y ratio of Ga_xAs_y . With the current UPS work the change in EA is quite evident when spectra are taken from differing regions of the composition-broadened mass peaks for any particular cluster size. For example, Figure 14 shows the UPS patterns obtained for the 23 atom clusters at the masses approximately corresponding to (x,y) composition values of (18,5), (12,11), and (5,18), respectively. The variation in apparent vertical EA for these clusters is nearly 0.5 eV. Similar results are obtained from spot checks of the composition variation of EA made for a number of clusters. Although this variation in EA across compositions for a single cluster size is within a factor of two as large as the observed even/odd variation between different cluster sizes, it is always found to be monotonic, and the even/odd alternation in EA is always evident as long as clusters of similar x/y composition ratios are compared.

The electron affinity of gallium arsenide clusters plotted in Figure 11 approaches quite rapidly to the bulk value of 4.07 eV. Clusters with about 50 atoms are already very close to this value. Even taking our energy resolution into account, the rate that the EA approaches the bulk value is still much faster than is typical with metal clusters such as potassium [33] or copper [34].

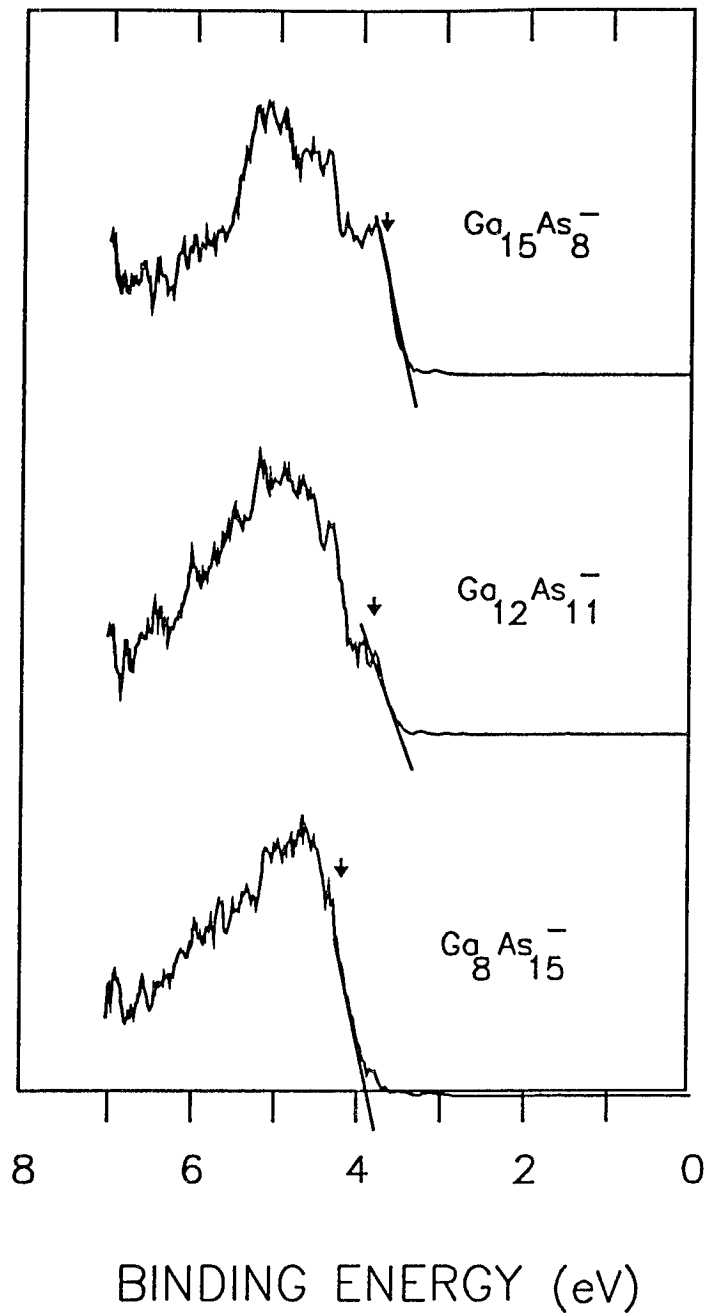


Figure 14. Photoelectron spectra of 23 atom Ga_xAs_y⁻ clusters at the masses approximately corresponding to (x,y) compositions of (18,5), (12,11) and (5,18), respectively.

Using semiclassical model treating the clusters as uniformly charged spheres, Brus [36] predicted that semiconductor clusters containing thousands of atoms still should have electron affinity a few tenths of an eV lower than the bulk value. This model clearly disagrees with the above observation. Studies of GaAs clusters in liquid quinoline [37] show also a smaller change in the energy gap between the occupied and unoccupied states than predicted by this semiclassical model. For the cluster size range under study here, it is no longer possible to ignore the influence of atoms on the cluster surface [38]. In reality, the extra electron is apt to be concentrated near a few surface corner atoms rather than being distributed uniformly throughout the clusters. For even the most perfect possible macroscopic GaAs crystal the corners between otherwise perfectly reconstructed surface facets will act as shallow traps slightly below the bottom of the bulk conduction band. These corner traps are likely sites for localization of the excess charge of the negative ion. To the extent the charge is localized, it will not take a very large cluster to mimic this effect. Interestingly, near-IR spectra of InP clusters measured by Kolenbrander and Mandich [39] exhibit a distinct continuum absorption with an onset of 1.3-1.5 eV, close to the band gap of bulk crystalline InP. For a variety of reasons, therefore, these small nano-meter-scale clusters may be quite adequate models of much of the physics and chemistry that occurs on the surface of bulk gallium arsenide.

Chapter Three

Shell Closing in Metal Cluster Plus Adsorbate Systems

3.1 Jellium model of metal surfaces

Metal surfaces have attracted attentions from both the experimental and theoretical scientists for quite a long time [40]. As a result many theoretical methods of calculating surface properties have been developed. Among them one-electron model views the solid as an electron moving in a periodic potential of positive ions and average interaction of all the other electrons. The most desired way to obtain the electronic structure of surfaces is to obtain the exact form of the periodic potential and do a detailed calculation to solve the appropriate one-electron Schrodinger equation. Unfortunately, this task is very tedious and computer-intensive if not impossible, and, therefore, simple models for the periodic potential need to be provided.

For the case of simple metals, conduction electrons are scattered only very weakly by the positive ion cores so that the whole solid system can be viewed as electrons interacting with a homogeneously distributed, positively charged background. The ion-electron interaction can be replaced by the potential created by this charge distribution. Because of the uniform background, this model is often called the jellium model. At metal surfaces, the charge density of the semi-infinite ion lattice is expressed as:

$$n(r) = \begin{cases} n & z < 0 \\ 0 & z > 0 \end{cases} \quad (6)$$

where z is the distance normal to the surface.

The jellium model has been very successful in describing a wide variety of metal surface properties. For example, it has been used to estimate work functions and certain chemisorption reactions.

3.2 Cluster Analog of the Surface Jellium Model -- Cluster Shell Model

Clusters have fewer atoms than the bulk solids. For small clusters, the most accurate way to calculate their properties is to first obtain the structure of the cluster by minimizing the total energy of the system, then take a high level theoretical *ab initio* approach. However for larger clusters this would require tremendous computation time, and with currently available computational resources it is nearly impossible except for clusters with high symmetry like C_{60} .

Just like the case of simple metal bulk surfaces, interactions between electrons and ions in simple metal clusters are weak. Geometrical structures of these clusters are less important compared to other clusters, *e.g.* semiconductor clusters. Jellium models developed for bulk metal surfaces may also be appropriate for metal clusters. The jellium model for metal clusters was first proposed by Knight and co-workers [41]. This model describes the metal cluster electronic structure by only considering the valence electrons moving in a smooth jellium like potential. Knight *et al.* initially used the Wood-Saxon central field potential

$$V(r) = -V_0 / \{[\exp(r - r_0) / \epsilon] + 1\} \quad (7)$$

and later they also explored perturbed harmonic oscillator and rectangular well potentials. Many of the jellium model results were found insensitive to the exact form of the central field potential.

One common feature for central field potentials is that we can separate the Schrodinger equation into radial and angular parts. The wavefunction can be written as

$$\Psi_{nlm}(\mathbf{r}) = F_{nl}(r)Y_{lm}(\theta, \varphi) \quad (8)$$

where $F_{nl}(r)$ is only a function of r determined by the specific central field potential. $Y_{lm}(\theta, \varphi)$ is a spherical harmonic. n, l, m are quantum numbers of the wavefunction. This results different energy levels, i.e. different eigenvalues of the Schrodinger equation, corresponding to different quantum numbers n, l , and m . For a non-coulombic potential, l can be any positive integer for a given n . Therefore we would have energy levels 1s, 1p, 1d, 1f, ... 2s, 2p, 2d, 2f, ... *etc.*, with each level being $2l+1$ degenerate. Because of this shell like energy level structure, the jellium model for clusters is also called the shell model. The energy level order varies on different potentials. The Woods-Saxon potential gives

$$1s < 1p < 1d < 2s < 1f < 2p < 1g < 2d \dots$$

resulting in electronic shell closings at

$$2, 8, 18, 20, 34, \dots$$

The cluster shell model successfully predicted and explained the major magic numbers in the mass spectra of alkali metal clusters. Every alkali atom can be considered to contribute one s-electron as a conduction electron. Shell

model predicted these alkali metal clusters should be stable for $N=2, 8, 18, 20, 40$ etc. and it was so observed in the mass spectra.

However, the minor magic number mass peaks of the alkali metal clusters, e.g. $N= 12, 14, 26, 30...$ can not be understood from the spherical jellium model. Actually, open shell clusters would prefer ellipsoidal structure as indicated by detailed calculations [42] in which the clusters are allowed to distort with a constant volume to obtain the minimum energy. A modified 3D harmonic oscillator potential has been used by Saunders to get energy levels for an ellipsoidal cluster [43,44]. There are three characteristic frequencies, and smaller potential curvature along an axis results lower corresponding frequency. If the cluster distortion are constrained to occur at constant volume, the frequencies are related by [43]

$$\omega_x \omega_y \omega_z = \omega_0^3 \quad (9)$$

The energy levels of this ellipsoidal model agree well with experimental alkali metal cluster abundance spectra and naturally include the major peaks of the spherical model.

Noble metals, with closed d-shells, are also monovalent. Pettiette *et al.* [45] measured the ultraviolet photoelectron spectra of Cu cluster anions and obtained the electron affinities and HOMO-LUMO gaps. The results were in good accord with the prediction of the ellipsoidal shell model. Later on, these measurements were extended to the other noble metals, namely Ag and Au [23]. Again, the cluster jellium model appeared to explain the experimental results.

3.3 Metal Cluster Plus Adsorbate Systems

Previous cluster shell model studies have been concentrated on systems where the delocalized electrons are all from metal atoms themselves. Little or no data are available for studies of the shell closing effects in metal cluster plus adsorbate systems, like Cu_xCO . In the case of CO reacting with transition metals, CO will donate the 5σ electrons to the metal, and the metal will back donate its d-electrons to the 2π antibonding orbital of the CO to complete the chemisorption [46,47]. For the noble metal Cu, the d-shell is closed and there is little direct experimental evidence to support the backbonding of CO on copper surfaces. There may be some back donation from neutral Cu clusters to CO to avoid too much charge buildup on the Cu cluster [48], but it is obviously not necessary for Cu cluster cations. Therefore we can say that CO is chemisorbed on Cu clusters by donating the 2 5σ electrons to Cu.

Will the 2 electrons from the CO ligand contribute to the shell closing of the system? From a theoretical cluster modeling point of view the answer to this question is of key importance. Siegbahn and coworkers [49] studied theoretically the chemisorption energy as a function of cluster size for adsorbates like hydrogen, oxygen, fluorine, methylene and methyl. They found that for all these adsorbates, a good agreement between the cluster model and infinite surface results is obtained if the electrons of the adsorbate fit into the electronic structure of the bare cluster, which means that the electrons from the adsorbate occupy part of the cluster orbitals. This picture of chemisorption predicts that electrons from the ligand and electrons from the metal clusters contribute together to shell closings in the metal cluster plus adsorbate systems.

In organometallic chemistry electronic shell closings have always played a significant role in the rationalization of the stabilities of certain transition metal

complexes. The most well known of these shell closing effects is the 18 electron rule which explains the stability of large numbers of metal complexes, for example metal carbonyls like Ni(CO)_4 , Fe(CO)_5 and Cr(CO)_6 . These shell closings occur around the transition metal atom and it is in this context important how the ligand electrons are counted. For CO only two electrons, the carbon lone pair electrons, are considered to contribute to the shell closing around the metal atom.

Table II. Chemisorption of CO on singly ionized and neutral copper clusters, energies in eV.

Cluster	Neutral	Cation
Cu ₁	0.10	1.18
Cu ₂	0.60	1.06
Cu ₃	0.93	1.00
Cu ₄	1.03	1.04
Cu ₅	0.46	1.19
Cu ₆	1.06	1.23
Cu ₇	0.59	1.42
Cu ₈	0.44	0.93
Cu ₉	0.72	0.88
Cu ₁₀	0.31	0.66

Theoretic calculations for the neutral and cationic Cu_xCO systems were carried out by Siegbahn's group [50]. In their calculations the valence electrons were correlated using the size-consistent modified couple pair functional (MCVPPF) method [51] based on self-consistent-field (SCF) orbitals. The results of the calculations for the chemisorption energy of CO on neutral and cationic copper clusters up to 10 atoms are given in Table II. The most important result in this table is that the energies have clear maxima at Cu_6CO for the neutral clusters and at Cu_7^+CO for the cationic clusters. The simple explanation for these results is that shell closings including 8 electrons have occurred for these cluster systems, where 6 electrons come from the cluster and 2 electrons come from CO. The shell closing effect is particularly marked if these clusters are compared to larger clusters, for which the CO lone pair electrons have to be added to an orbital outside the closed shells. The effect is less marked in a comparison to smaller clusters since the lone pair electrons can then be added to the unfilled 1p shell of the cluster. Also, for the smaller cationic clusters there is a compensating effect in that CO gets closer to the delocalized positive charge on the cluster. For the smallest system with only one atom this positive charge leads to a very large difference compared to the neutral system, whereas for the largest systems studied the additional binding due to the charge is less marked.

The shell closing effect occurring for the cations at Cu_7^+CO is clearly seen also in the calculated LUMO energies of the bare clusters listed in Table III. There is an increase in the virtual orbital energy of about 1 eV between Cu_7^+ and Cu_8^+ as a result of the shell closing. A picture of the chemisorption of CO where the carbon lone pair electrons add in the LUMO is the obvious

rationalization for the correlation between the absolute values of the LUMO energies and the association energies in Table II.

Table III. Calculated LUMO energies of the bare Cu^+ clusters.

Cluster	LUMO Energy (eV)
Cu_5^+	-4.4
Cu_6^+	-4.1
Cu_7^+	-4.4
Cu_8^+	-3.1
Cu_9^+	-3.2

The rates of association reactions between cationic copper clusters and CO have already been studied recently by Leuchtner, Harms, and Castleman [52]. No indication of shell closing effects were noted. This was in sharp contrast to their earlier results on O_2 reactions with aluminum cluster ions [53] where such closed-shell species as Al_{13}^- (40 valence electrons) were found to be strikingly inert. We suspect their inability to observe shell closing effects in the $\text{Cu}_x^+ + \text{CO}$ experiments was due to the absence of a substantial activation barrier to reaction. Under their relatively high pressure, low temperature experimental conditions, all clusters larger than 5-7 atoms reacted, and there was little ability to differentiate one chemisorbed cluster from another. Therefore, it is highly desirable to perform a set of new experiments that focus on relative

binding energies rather than reaction rates as a function of cluster size. They should provide a more direct test of theoretical predictions of stability.

3.4 FT-ICR Experimental

Experiments on metal cluster plus adsorbate systems in this group are performed on a Fourier transform ion cyclotron resonance (FT-ICR) cluster beam apparatus [54,55]. It consists of cluster generation, injection, trapping, excitation and detection systems. The apparatus is shown in Figure 15.

Cluster generation is the same as that described in the UPS section. They are prepared by laser vaporization of a copper target disk in a pulsed supersonic nozzle, and cooled in a supersonic expansion. This nozzle has a 0.3-cm-i.d., 1.0-cm-long cylindrical "waiting room". The clusters are formed and thermalized in this "waiting room" zone of the nozzle. The clusters then pass through a 2.0-cm-long conical expansion cone, with a 0.15-cm-i.d. entrance and 100° total internal angle. A 2.1-cm-long electroformed nickel skimmer at a distance of 8.4 cm down stream skimmers the central 0.2-cm-diameter section of the cluster beam.

The source chamber used in the FT-ICR apparatus, shown in Figure 16, is a lot more compact than the one used in the UPS apparatus. Since the clusters have to be cooled in the ICR cell later on, only one pulsed valved is used. The whole source chamber is built on a 6" o.d. conflat flange six-way UHV cross pumped by a 170 liter/s molecular turbo pump. The base pressure is in the range of 1×10^{-8} Torr. In operation with a helium carrier at 10 Hz with a 0.05

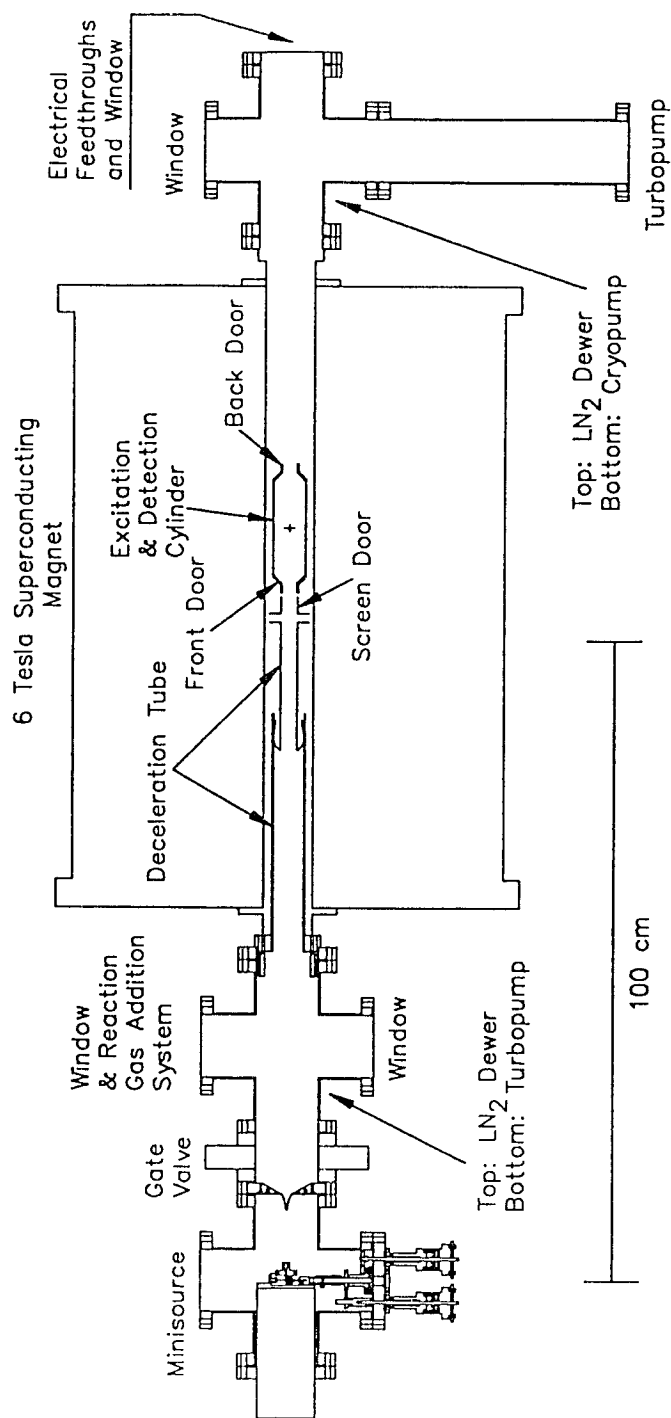


Figure 15. FT-ICR apparatus.

Torr/per pulse gas output, the average pressure in this source is roughly 4×10^{-3} Torr.

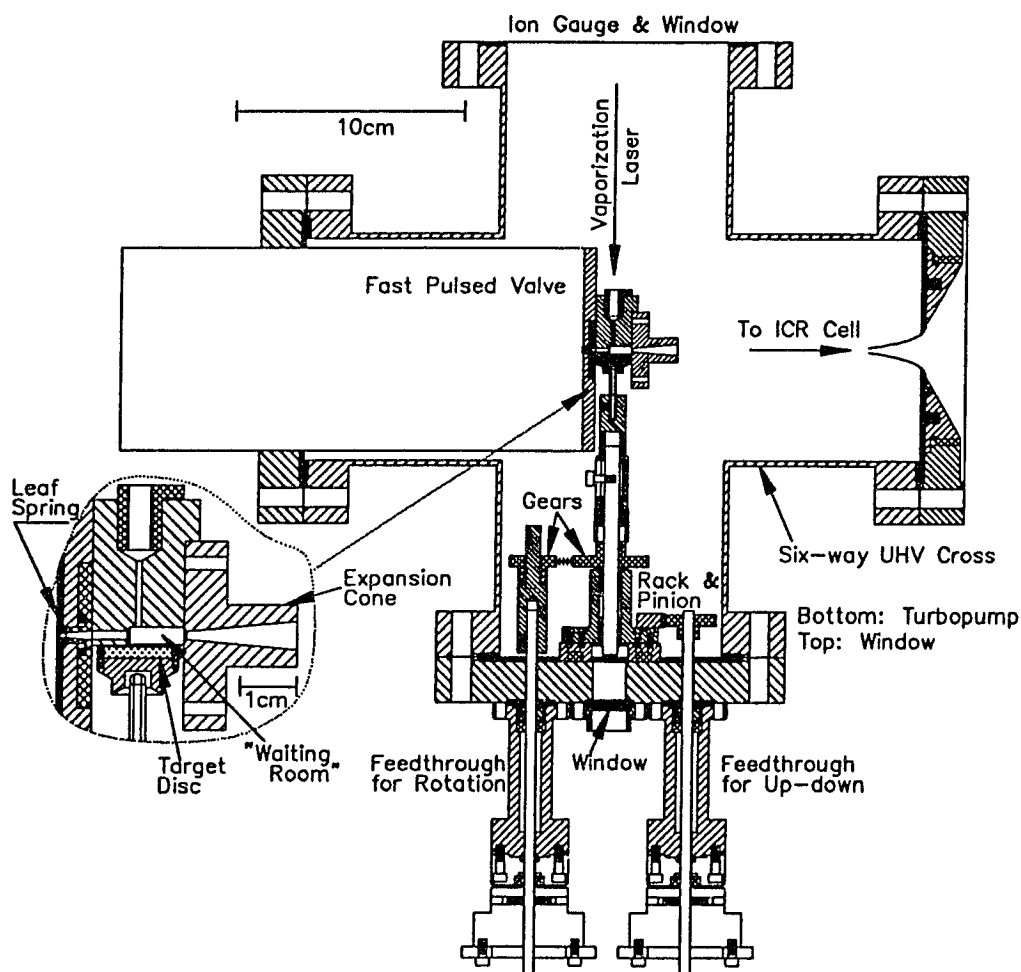


Figure 16. Cross section of the FT-ICR cluster source chamber.

The rest of the UHV chamber are pumped by two 170 liter/s molecular turbo pumps, one on each end of the superconducting magnet, and a 20-cm-i.d.

CTI cryopump located at the back end of the magnet. There is a butterfly valve controlled by a computer between the cryopump and the chamber. One ion vacuum gauge is located near each of the two turbo pumps. The base pressure of the system is in the range of 5×10^{-10} Torr. The pressure in the ICR cell which is located at the center of the magnet is estimated by taking the average of the two ion gauge readings.

The ICR magnetic field is provided by a 6-Tesla superconducting magnet. Charged particles entering from a low field region to a strong magnetic field will experience a magnetic mirror effect. This is because cluster ions traveling with large angles relative to the magnetic field will have most of the velocity parallel to the axis converted to velocities perpendicular to the axis. At certain point they will be stopped and turned back. To avoid this effect, the cluster beam is collimated by expansion nozzle cone and the skimmer to travel parallel to the axis of the superconducting ICR magnet. The charged cluster ions thus will follow the magnetic field lines to enter and be trapped in the ICR cell.

Clusters seeded in the He supersonic beam are all accelerated to nearly the same speed, roughly $V_0 = 1.9 \times 10^5$ cm/s. The kinetic energy of one particular cluster is linearly dependent on its mass. After the cluster beam passes the skimmer, it has to go through a deceleration tube before entering the ICR cell. For the positively charged clusters, after they are wholly inside the deceleration tube, the deceleration tube is pulsed to a negative potential $-V_1$. The potential at the screen door is pulsed from 10 V to ground when clusters exit the tube. The cluster cations will be decelerated after they travel out of the deceleration tube, which is held at $-V_1$, and get back to the ground potential at the screen door.

The cluster cations with kinetic energies less than eV_1 , with masses less than $2eV_1/V_0^2$, can not pass the screen door and enter the ICR cell.

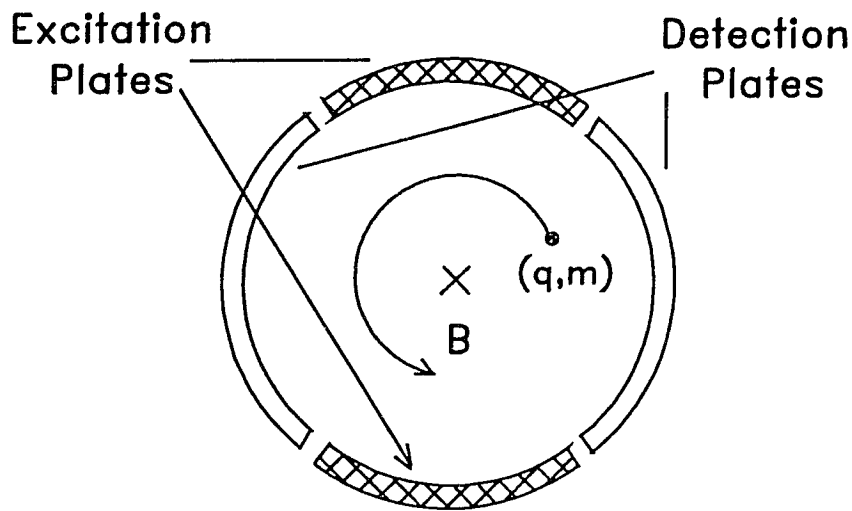


Figure. 17. Cross section of the ICR cell.

The ICR trapping cell is a cylinder, 15 cm long, 4.8 cm inside diameter. The cross section of the cell is shown in Figure 17. The sides of the cylinder are split longitudinally into four sectors: one opposing set of two 60° sectors are called excitation plates and used to apply RF power to excite the cyclotron motion, the second opposing set of 120° sectors are called detection plates and used for detecting the coherent ion cyclotron motion. These cylindrical sectors are fabricated from oxygen free high conductivity (OFHC) copper, polished and

silver plated with a final surface "flash" of rhodium in order to provide a clean corrosion-free surface with uniform surface potential.

A charged particle with charge q and mass m in a magnetic B will undergo cyclotron motion perpendicular to the field. The cyclotron frequency is given by

$$f_c = qB/m \quad (10)$$

The ions can not escape from the cell in directions perpendicular to the B field due to this cyclotron motion. The positive ions are trapped along the magnetic field axis by two end plates held at 10 V. These two plates are called "front door" and "back door" respectively.

As the clusters entering the cell, the front door is kept at 3V as to let most of them go through yet to prevent previously trapped, partially thermalized clusters from escaping the cell. The back door is kept at 10 V during the injection. Thus clusters with 3-10 eV kinetic energies after deceleration are trapped in the cell. By varying the deceleration voltage, we can selectively trap clusters with desired mass range.

This process is repeated for 30-50 times at a 10 Hz repetition rate. At the end, the front door potential is raised to 10 V, and Ar gas is introduced into the cell at 4×10^{-6} Torr for 3 seconds. The cluster ions are thus thermalized to room temperature by colliding with the Ar gas. The thermalization is necessary to prevent trapped ions from escaping the cell and to have a proper excitation and detection. It also assures that measurements for different injections are done at the same cluster temperature.

Initially the ions are located around the center axis of the cell. They can be excited to larger cyclotron orbitals by applying a RF field between the two excitation plates. The RF field can be expressed as

$$E(t) = E_0 \cos w_c t \mathbf{j} \quad (11)$$

As the ions speed up, their orbital radius r will increase as a function of excitation time t

$$r(t) = E_0 t / 2B_0 \quad (12).$$

where B_0 is the magnetic field. It is clear from Equation 12 that the orbital radius r of the excited ion is independent of m and q . Thus all ions of a given m/q range can be excited to the same cyclotron orbital radius by a RF field with constant amplitude over the frequency range. Only those ions with cyclotron frequencies the same as those of the RF field are excited. The cyclotron frequency of the ion is related to its mass according to Equation 10. We can selectively excite ions within certain mass range by applying an excitation RF field in resonance with those ions. The technique used in this group for ion excitation is called SWIFT (Stored Wave Inverse Fourier Transform) [56,57]. First one drafts a power spectrum which has uniform RF power over the range of cyclotron resonances appropriate to the desired cluster mass range, but zero RF power elsewhere, then takes the inverse Fourier transform of this power spectrum and generates a voltage wave form from the resulting time domain data array using a fast digital to analog converter (DAC) and applies it to the two excitation plates.

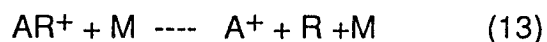
Often certain mass peaks in a mass spectrum interfere with a desired experiment. For example, if we want to study the photofragmentation of C_{60} , original mass peaks due to fullerenes smaller than C_{60} make it difficult to identify

the fragmentation products. It is desirable to remove these smaller fullerenes from the cell before fragmentation. One of the important applications of this very powerful SWIFT technique is to selectively remove unwanted trapped ions out of the cell while keeping the desired ions. In our experiments, after the trapped ions get thermalized, the cryopump valve is opened for about 3 seconds to bring the chamber to the 10^{-9} torr pressure range. We then apply excitation field over the resonance frequencies of the unwanted clusters with enough power and for a sufficient time period so that their cyclotron orbitals become so large that they collide with the side plates of the cell and are effectively removed from the cell. Ar gas is pulsed into the cell afterwards to make sure that the ions with masses not in resonance with the RF field get well thermalized and trapped in the cell.

Most of the cluster FT-ICR studies in this work involve chemical reaction of trapped cluster ions with a particular reactant gas. The reactant gas is added through a Jordon pulsed valve the same as the one used in the nozzle. After the cluster ions are trapped and thermalized, the valve is opened at a rate of 10Hz for the entire reaction period. The pressure is monitored using the two ion gauges.

Electrical feedthroughs are mounted on a 6" flange at the back end of the chamber. There is a small quartz window at the center of this flange through which laser light can pass through. When the trapped cluster ions are irradiated with laser light, they are heated to higher internal temperature. At certain point, this will cause fragmentation of the clusters. Photofragmentation experiments are carried out in this experiment using a XeCl laser (308 nm) at repetition rates of 10-50 Hz for 1-5 seconds.

Another way to cause the clusters to fragment is by collision of the accelerated ions with an inert gas. This is so called collision induced dissociation (CID). The process can be expressed as:



where AR^+ is the cluster cation before dissociation, A^+ and R are dissociation products, and M is the rare gas atom. Freiser and co-worker [58] first performed CID experiments in a FT-ICR spectrometer in 1982. In the experiment described below the kinetic energy of the cluster ions under study is increased by applying a RF field to the excitation plates and exciting the ions to larger orbitals. The energy gained in the laboratory frame during the resonance excitation is given by [59]:

$$E_l(t) = (qE_0t)^2 / (8m_a) \quad (14)$$

where m_a is the cluster ion mass. The kinetic energy of the cluster ions is changed by altering the RF field amplitude while keeping the excitation time constant. Then Ar gas is introduced into the cell. The relevant energy during the two-body collision is the kinetic energy in the center-of-mass frame E_c :

$$E_c = E_l m_r / (m_r + m_a) \quad (15)$$

where m_r is the rare gas atomic mass. The cluster ions are allowed to interact with the target gas (Ar) for a certain period of time, and the dissociation of the ions occurs during this period. Hop *et al.* [59] showed that the RF excitation of ions in the FT-ICR cell produced ions with a narrow and well defined kinetic energy, and it has been used to determine bond dissociation energies.

After all of the measurements are done on the trapped ions, next step is to look at what is left in the cell by taking a mass spectrum of the ions. The pressure of the chamber is first brought to the range of 10^{-9} Torr by pumping out

the rare gas and the reactant gas. The ions are excited to a larger orbital which is very close but not touching the two detection plates. The image current between the two plates induced by these ions is differentially amplified by a sensitive preamplifier (Stanford Research Systems SR 560). The gain of the amplifier is usually set at 5×10^3 to 1×10^4 . The amplified signal is then heterodyned with a mixing frequency or directly sent to a transient digitizer and passes through a CAMAC interface to a workstation, where the data are Fourier transformed to give a mass distribution of the ions in the cell. To increase the resolution of the mass spectrum, the same number of zero's as the original data are added at the end before the Fourier transform process.

The whole process is under computer control. Part of the work (CID experiment of Cu_x^+CO) presented here uses a IBM AT personal computer to synchronize the experimental steps through the CAMAC interface (Kinetic Systems, model 1502), and the data processing is done using a Digital Equipment Corporation μVAX workstation. An array processor (CSPI MAP 4000, speed 40 Mflop) is connected to the μVAX workstation to perform the fast Fourier transform. We updated the system later on, and now both the experimental control and data processing are integrated into an IBM RISC/6000 POWERstation 320. The program is written in C under X window environment using the AIX operating system [60].

As a summary, one typical ICR experiment cycle involves the following steps (for positively charged cluster ions):

1. Dump The potentials on the side plates, front door and the back door are changed to -10 V for 3 seconds to extract the previously trapped ions in the cell.

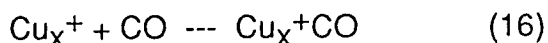
2. Inject 10-100 cycles of cluster ion generation, injection, and trapping to fill the cell with cluster ions of desired masses (see detailed procedures in previous paragraphs).
3. Thermalize Ar gas is pulsed into the cell for 3 seconds to thermalize the trapped cluster ions.
4. Pump The Cryopump valve is opened to bring the chamber pressure to 10^{-9} Torr range by pumping the thermal gas out.
5. Eject Apply a RF field to eject unwanted ions out of the cell, followed by thermalization.
6. ZAP Radiate trapped ions with laser light at 10-50 Hz, followed by thermalization.
7. React Introduce a reactant gas into the cell for a certain time at a controlled pressure.
8. CID First execute step 4 (Pump), then excite the ions to higher translational energy with a controlled excitation time and power and let them collide with Ar gas introduced into the cell after excitation.
9. Pump Repeat step 4 to evacuate the cell to prepare for excitation and detection.
10. Look Excitation and detection. Perform Fourier transformation and plot the mass spectrum on the computer screen.

3.5 Results and Discussion

3.5.1 Noble Metal Clusters

The top panel of Figure 18 shows the observed mass spectrum of the copper clusters as initially injected. Here the injection parameters are chosen to select only those copper clusters in the size range from 6-12 atoms. The middle panel shows the change in this mass spectrum brought about by a 1.1 second exposure to CO reactant gas at 1×10^{-6} Torr. The formation of chemisorbed products having one CO attached to the cluster is evident here for all Cu_x^+ clusters, although it is clear that Cu_7^+ has the greatest effective reactivity at these pressures. The effect of chemisorption of a small amount of background H_2O is also evident in this panel for some of the clusters.

The chemical reaction process here can be expressed in a simple form



for which the reaction rate is

$$d[\text{Cu}_x^+] / dt = -k_x [\text{Cu}_x^+] \quad (17)$$

The concentration of CO is much excessive compared with Cu_x^+ so that it is considered as a constant and is incorporated into the rate constant k_x . Integration on both sides of Equation 17 over time t gives an expression for k_x

$$k_x = -t^{-1} \ln I_x \quad (18)$$

where

$$I_x = [\text{Cu}_x^+] / [\text{Cu}_x^+]_0 \quad (19)$$

is the measured unreacted fraction of Cu_x^+ , and $[\text{Cu}_x^+]_0$ is the control concentration. We know approximately the pressure of CO in the chamber and the reaction time, therefore we can calculate the rate constant by fitting a line

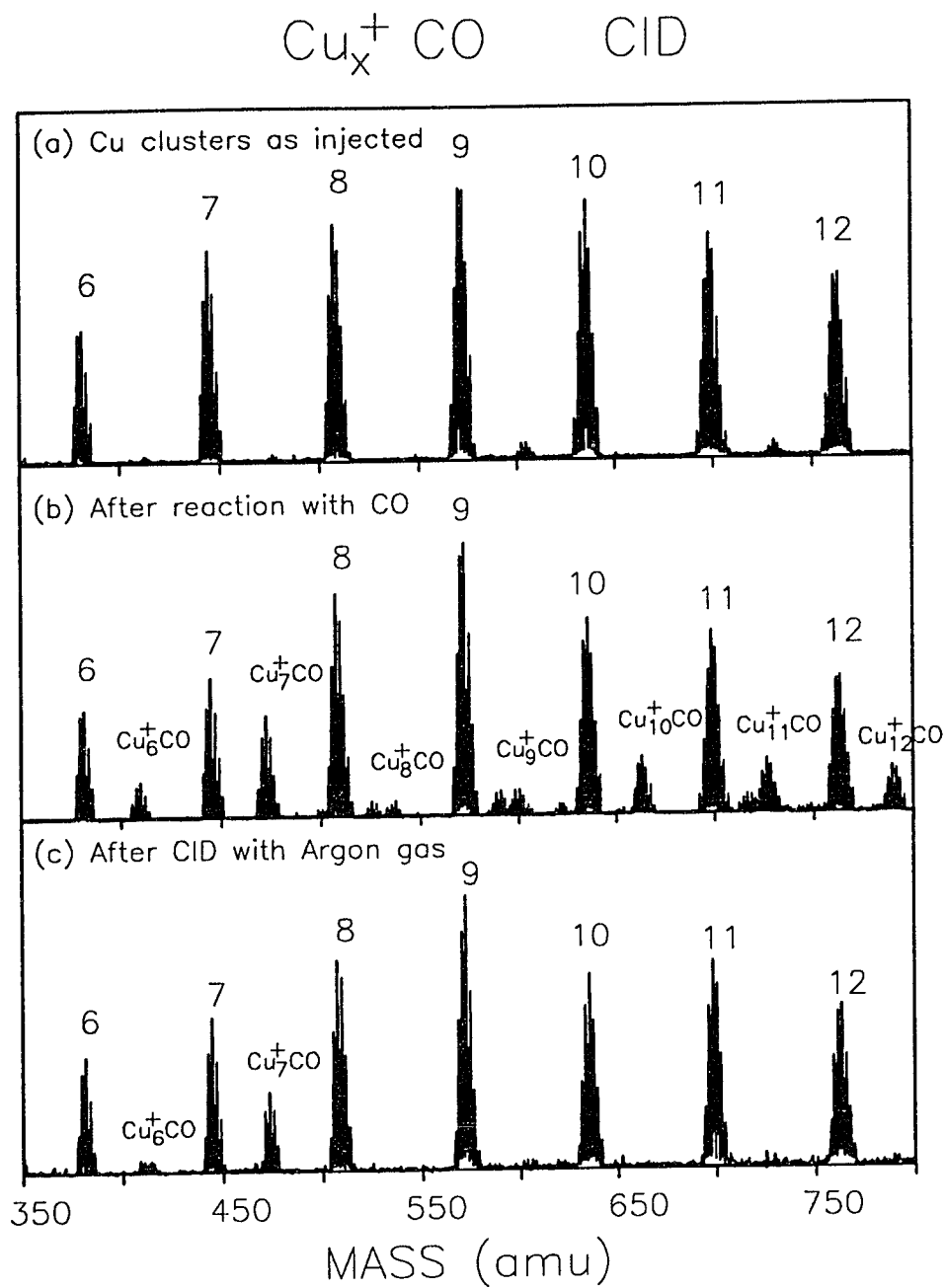


Figure 18. CO chemisorption experiment on copper cluster cations in 6-12 atom range: (top) mass spectrum of Cu_x^+ as injected into FT-ICR trap, (middle) mass spectrum after exposure to CO reactant gas at 1×10^{-6} torr for 1.1 seconds, (bottom) resultant FT-ICR mass spectrum after CID with argon at 1×10^{-6} Torr. Note the special stability of $\text{Cu}_7^+ \text{CO}$.

to the log of the measured Cu_x^+ concentration ratio. However in this study of the shell closing effect of the metal cluster plus adsorbate systems, what is most important is the relative reactivity and the relative bonding energy between Cu_x^+ and CO, and we have far more confidence in taking the ratio of Cu_x^+ to that of a

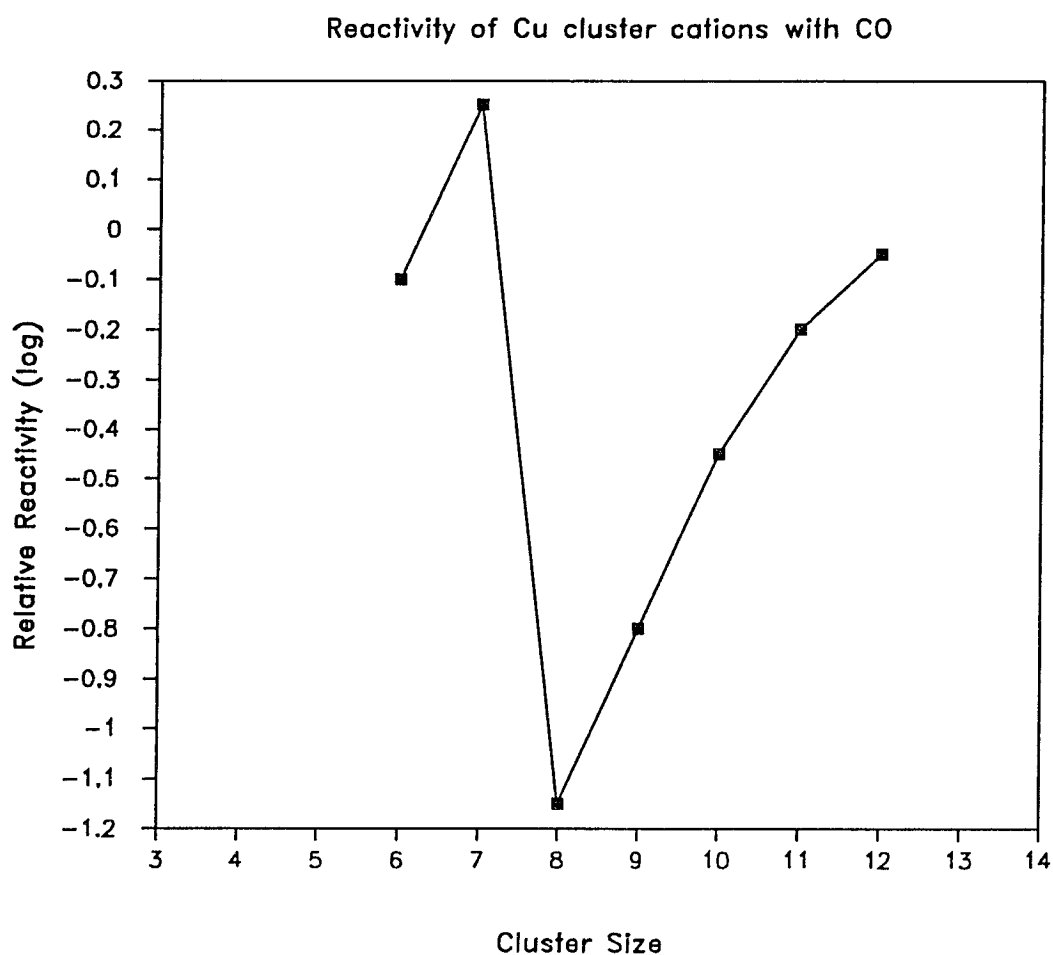


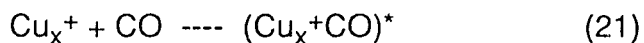
Figure 19. Relative reactivity of Cu_x^+ with CO.

reference cluster measured in the same experimental cycle. The relative reaction rate is given by

$$R_x = \ln I_x / \ln I_r \quad (20)$$

where I_r is the unreacted fraction of the reference cluster. R_x is measured for copper cluster cations between 6-12 and averaged for different reaction time t , and is plotted in Figure 19. Care has been taken to make sure that there is only one CO attached to each Cu_x^+ after reaction. Figure 19 clearly shows that Cu_7^+ is most reactive towards CO in this cluster size range.

In principle we can obtain information on bonding energies between Cu_x^+ and CO based on the reactivity data using the RRKM theory. The chemisorption reaction for Cu_x^+ with CO is assumed to be steady state and pseudo first order and to proceed according to the Lindemann mechanism. The simple expression in Equation 16 actually involves several steps. First an ion-molecule complex $(\text{Cu}_x^+\text{CO})^*$ is formed with a rate constant k_1 due to collisions between Cu_x^+ and CO. The complex $(\text{Cu}_x^+\text{CO})^*$ could undergo unimolecular decay with a rate constant k_{-1} . It also could be stabilized by a collision with a third body R, most likely Ar but can also be another CO molecule, with a rate constant k_2 . The process can be expressed as:



The over all reaction rate constant can be written as

$$k = k_1 k_2 / (k_{-1} + k_2[\text{R}]) \quad (23)$$

The CO concentration is considered as a constant and is incorporated into the rate constant k_1 . k_1 can be calculated using the Langevin collision rate [61]. k_2 can be estimated from the collision rate and stabilizing factor of the rare gas.

We know the pressure of R (Ar) and CO, the back dissociation rate constant k_{-1} thus can be derived from Equation 23 using the measured reaction rate constant k . The back dissociation process is a unimolecular decay process, and the bond energy can be calculated using RRKM theory with the known dissociation rate constant k_{-1} .

Although the RRKM theory could give an estimate of the bond energy from the reaction rate as described above, there are several unknown adjustable parameters that have to be estimated in the calculation. The most direct measure of the relative stability of these clusters is provided by the results of the CID experiment. Here all clusters and their reaction products throughout this region of the mass spectrum are excited in the presence of argon buffer gas. After thermalization, all the chemisorbed species have desorbed from the clusters except Cu_7^+CO and Cu_6^+CO , as revealed by the FT-ICR mass spectrum plotted in the bottom panel of Figure 18. Define a mass peak ratio between after and before the CID

$$\text{MR}_x = [\text{Cu}_x^+\text{CO}]_{\text{CID}} / [\text{Cu}_x^+\text{CO}]_0 \quad (24)$$

where $[\text{Cu}_x^+\text{CO}]_{\text{CID}}$ is the peak height of Cu_x^+CO after CID and $[\text{Cu}_x^+\text{CO}]_0$ is that of before CID. Clearly MR_7 is the highest in this region, indicating that Cu_7^+CO is the most stable compound. This is in excellent agreement with the calculated stabilities of Table II, and support the picture that electrons from the ligand will also contribute to the shell closing of the system.

The next electronic shell closing number is 18. Similar experiments in the 14-24 atom size range for positive copper clusters show that MR_{17} is the highest, suggesting that $\text{Cu}_{17}^+\text{CO}$, which has 18 valence electrons, is the most stable reaction product in this region. Here, however, the effect is found to

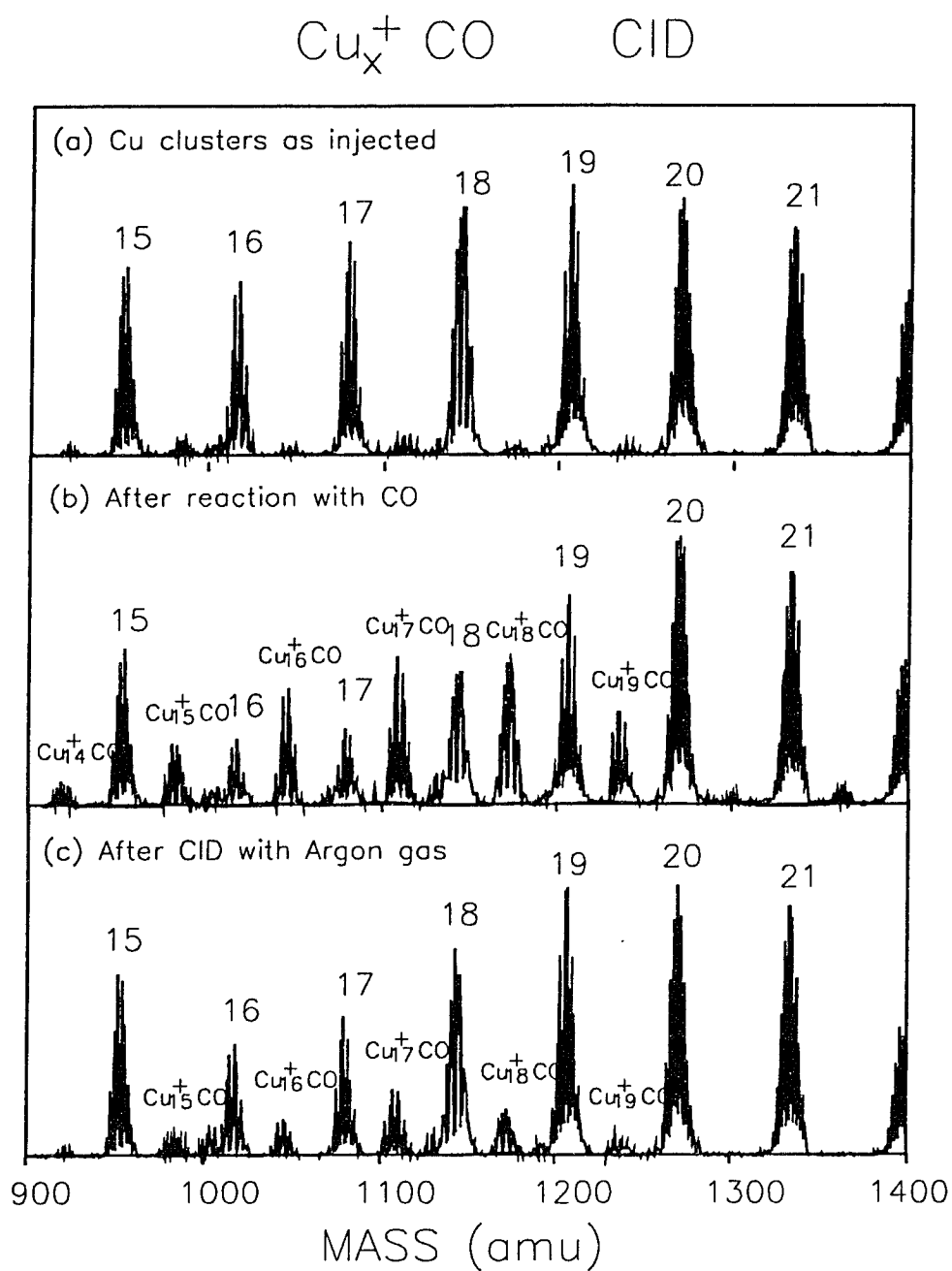


Figure 20. CO chemisorption experiment on copper cluster cations in 15-21 atom size range: (top) mass spectrum of Cu_x^+ as injected into FT-ICR trap, (middle) mass spectrum after exposure to CO reactant gas at 1×10^{-6} Torr for 1 second, (bottom) resultant FT-ICR mass spectrum after CID with argon at 1×10^{-6} torr. Note the special stability of $\text{Cu}_{17}^+ \text{CO}$.

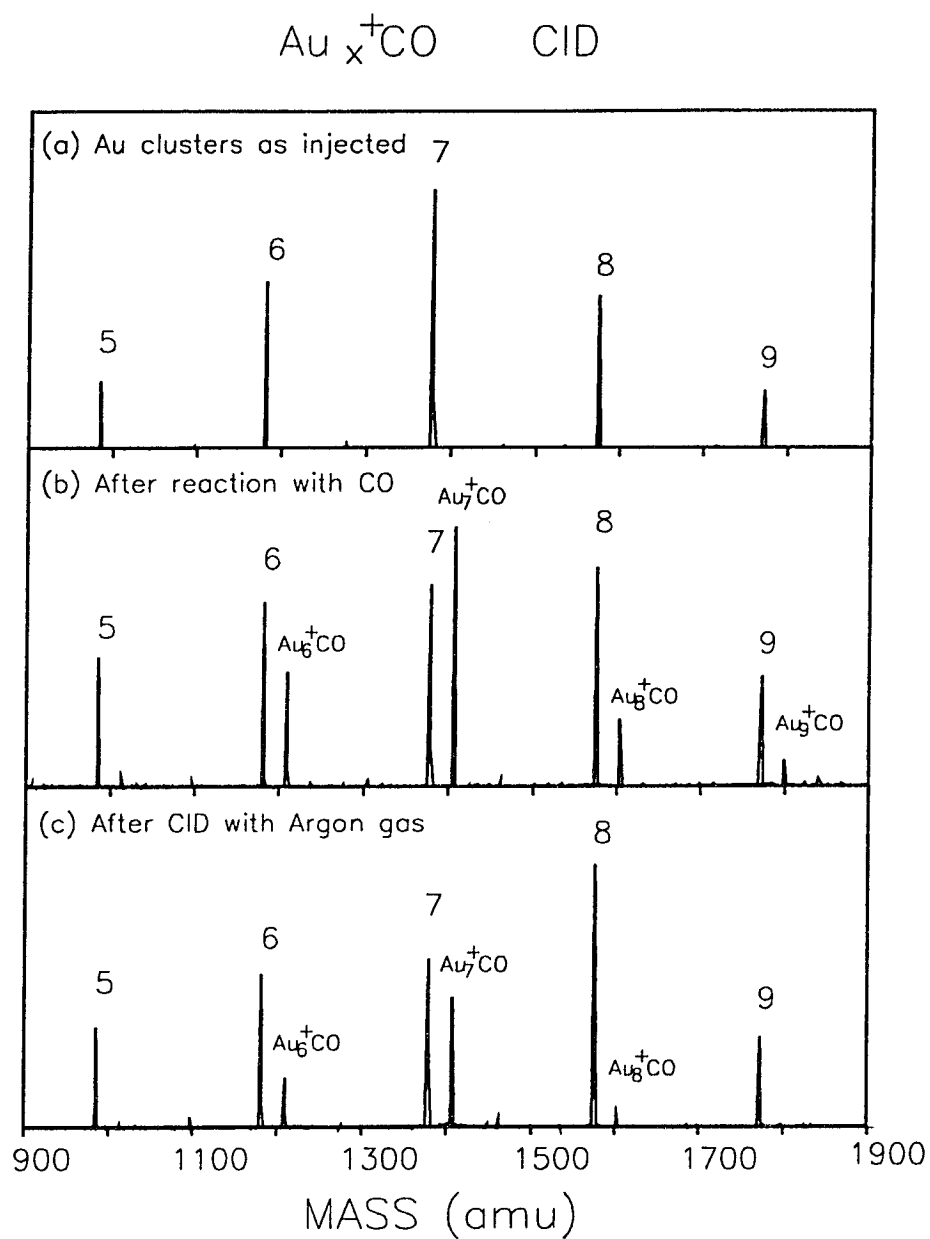


Figure 21. CO chemisorption experiment on gold cluster cations in 5-9 atom size range: (top) mass spectrum of Au_x^+ as injected into FT-ICR trap, (middle) mass spectrum after exposure to CO reactant gas at 1×10^{-6} torr for 0.5 seconds, (bottom) resultant FT-ICR mass spectrum after CID with argon. Note the special stability of Au_7^+CO .

be somewhat less clear than in the size range around Cu_7 . As shown in Figure 20, $\text{Cu}_{17}^+\text{CO}$ appears to be simply the maximum of a series of relatively stable clusters ranging from $\text{Cu}_{15}^+\text{CO}$ through $\text{Cu}_{19}^+\text{CO}$. Photoelectron spectra of the negative bare copper cluster ions in this size range [45] showed evidence for shell closing effects both at 18 and at 20.

More recent photoelectron spectroscopy studies of other coinage metal clusters [35] have shown the shell closing effects to be much more clear in this size range for gold. Here the closings at 8 and 20 electrons are dramatically evident. Accordingly, FT-ICR survey experiments for CO chemisorbed positive gold clusters similar to those of Figure 18 are found to reveal excellent accord with the expectations of the above simple theory: Au_7^+CO and $\text{Au}_{19}^+\text{CO}$ are quite evidently the most stable chemisorbed clusters. Figure 21 shows, for example, the result of a reaction and CID experiment in the vicinity of Au_7^+ .

3.5.2 Transition Metal Clusters

It will be interesting to see how far this concept of shell closing and the participation of extra electrons donated in the process of chemisorption will continue to be useful. Even in the more complicated case of transition metal clusters like Co_x with unfilled d band, it is still conceivable that the s/p electrons continue to exhibit shell structure. The shell closing may be manifest both in the reactivity of the bare cluster and the stability of their chemisorbed products.

We study the effect by measuring the reactivity of transition metal clusters with H_2 . Trying to understand the process of H_2 dissociative chemisorption on

transition metal surfaces, Harris and Anderson [62] proposed a model in which the controlling factor for the reactivity of H_2 on metal surfaces is the Pauli repulsion between the spatially diffused s-electrons of the metal and the σ bonding electrons of the hydrogen molecule. The dissociative reaction activation barrier is reduced in the case of transition metals by promoting the s-electrons of the metal to the more localized and unfilled d bands to avoid this Pauli repulsion. For transition metal clusters, if the s-electrons still behave like shell electrons, the s-band (orbitals) should move lower in energy when the electronic shell is closed. According to the Anderson-Harris model, this will raise the s to d promotion energy, creating higher activation barrier for the H_2 chemisorption. Therefore transition metal clusters with closed electronic shell should be least reactive toward H_2 .

The relative reactivity of Co_x^+ and Co_x^- with H_2 are measured in the same way as that of Cu_x^+ reaction with CO, except that the ICR cell is cooled with liquid nitrogen to eliminate H_2O contamination. Figure 22 shows the relative reactivity of Co_x^+ , Co_x , and Co_x^- with H_2 and D_2 . The neutral Co_x data is from ref 63. There are two reactivity minima in all three cases, one in the range of 6-9 and the other at the range of 19-21. These are the ranges that we would expect the shell closing to occur, and based on the Harris-Anderson model these clusters should be least reactive toward H_2 . Thus the reactivity minima are nicely explained by invoking the shell closing and the Harris-Anderson model.

The other evidence for the shell structure of Co_x clusters from the reactivity data is that the reactivity minimum in the 19-21 atom size range is shifted by one atom as one goes from positive to neutral, and from neutral to

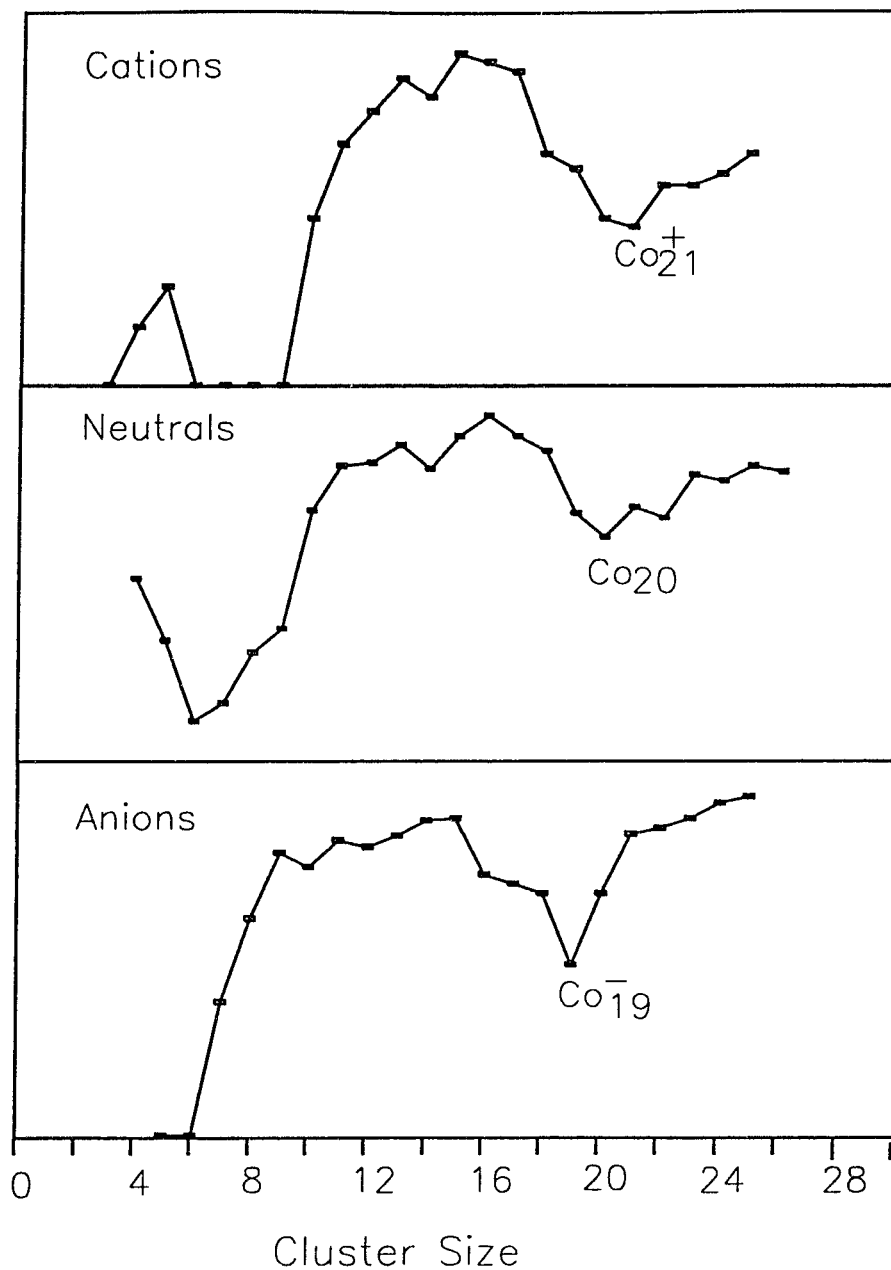


Figure 22. (top): Relative reactivity of Co_x^+ with H_2 measured with FT-ICR; (middle): Relative reactivity of Co_x with D_2 measured with a fast-flow device [63]; (bottom): Relative reactivity of Co_x^- with H_2 measured with FT-ICR. Note the two reaction minima occurred in all three cases, and the exact least reactive cluster sizes around 20 atoms.

negative. If we count one s-electron per Co atom, all the minima occur at 20 s-electrons, exactly a shell closing number. We find similar behavior for the different charge states of iron clusters also, but the minima do not occur at 20 or 18 indicating some iron atoms may contribute more than one electrons to the shell structure due to the s-d electron mixing. Because of this s-d electron mixing, the shell closing effects in transition metal clusters are generally less marked compared with those of simple and noble metal clusters.

Chapter Four

Doped Fullerenes

4.1 Fullerenes and Their Derivatives

In previous chapters, we mainly discussed common grounds between clusters and bulk surfaces, and showed that clusters can be used as models of real bulk surfaces. Since the size and formation environment are different from that of bulk materials, clusters themselves may form a new class of materials.

C₆₀ is the best example. It was discovered in Smalley group at Rice University in the course of laser vaporization supersonic beam studies of carbon clusters. The C₆₀ peak was found most abundant in the mass spectra. In their classical Nature article [8], the Rice group proposed the famous truncated icosahedral structure, shaped like a soccer ball, for C₆₀ and named it buckminsterfullerene. Larger carbon clusters were found also to have caged structures, with C₇₀, C₈₄, *etc.* being special. These new cage structured carbon molecules are referred as fullerenes. In 1990, Kratschmer, Huffman and coworkers found a simple method to generate macroscopic amount of these materials [9]. These fullerenes form the third form of carbon, besides planar graphite and tetrahedral diamond.

The reason that, in the process of laser vaporization or carbon arc, carbon forms fullerenes rather than graphite or diamond is that they are formed in a different environment. The model originally put forward by this group for the formation of these cages [64], involved the rearrangement of growing graphitic

sheets so as to incorporate pentagons and thereby produce a curvature which would minimize the number of dangling bonds. As we have discussed elsewhere [10], this model nicely explained the role of the helium in the Kratschmer-Huffman recipe [9] for the production of C_{60} in good yield. In this model the critical factor governing the yield of fullerenes of size near 60 is whether clusters growing into this size range have an adequate opportunity to anneal to their most energetically favored form. If, as we suspect, this form is the one which follows what we call the "Pentagon Rule" (i.e. the one that has the largest possible number of pentagonal rings while avoiding adjacent pentagons) then the fantastically high yields of C_{60} reported recently [65] are readily understood. The C_{60} soccerball structure is the inevitable result of slavish adherence to this Pentagon Rule during the growth process. The optimum pressure of helium is then the one which permits the most effective annealing during the critical early stages of growth. It does this by controlling the density of small carbon radicals close to the vaporizing graphite rod where the temperature is still high. The uniform advantage of incorporating pentagons in the formation of fullerenes is due to the fact that it forces the network to curl, thereby decrease the distance between dangling bonds, allowing some of them to join to form good carbon-carbon sp^2 bonds. Of course, the disadvantage is that the "pi" network is no longer flat, and the degree of aromaticity of the resulting curled sheet will suffer as a result of the decreased overlap of the " $2p_z$ " orbital. But as long as there are no two pentagons sharing a edge, the curvature of at any particular carbon atom is not so severe. For any growing graphitic sheet in the 30-60 size range, we expect that the advantage of curvature to the sigma framework far exceeds the reduction in stability of the "pi" bonding. However, the ratio of the number of edge atoms (where the dangling bonds are at) to that

of center (non-edge) atoms is much smaller in the case of infinite graphitic sheet, the "pi" bonding is more important than the dangling bonds in terms of minimum energy, and therefore in a process that involves very high carbon density we would expect the formation of graphite rather than fullerenes. The determining factors are the size of the clusters and the formation process.

The versatility of the fullerenes has been grown rapidly ever since the initial discovery. Haufler *et al.* [66] reported the formation $C_{60}H_{36}$ through Birch reduction, where a hydrogen atom is attached to every non-conjugated carbon double bond. Also, British workers [67] from the university of Leicester, Southampton and Sussex have successfully produced macroscopic quantities of fully fluorinated buckyballs ($C_{60}F_{60}$). Hebard and coworkers [68] at AT&T Bell Labs mixed, or doped, C_{60} solids with potassium to produce a new metallic phase, K_xC_{60} fulleride. It reaches the maximum conductivity for $x=3$. When $x=6$, the material became an insulator. The most exciting result is that K_3C_{60} becomes a superconductor when cooled below $T_c=18$ K. This certainly has driven the fullerene studies to a new level of interesting.

There is one thing in common in the above mentioned work, they all leave the C_{60} carbon cage intact. Indeed, laser vaporization supersonic cluster beam studies have shown that carbon appears to be unique in its ability to form fullerene cages [69]. Silicon, for example, does not form strong enough double bonds to stabilize the 3-connected network of the cage. Silicon clusters in the 2-100 atom size range therefore show no tendency to favor even-numbered clusters, whereas in carbon this even/odd alternation is one of the hallmarks of fullerene production. Boron nitride has a stable crystalline phase made up of 2-dimensional hexagonal sheets much like graphite, leading to the suggestion that

fullerene-type cages may be formed from BN units. However, since all fullerene cages must contain 12 pentagonal rings, it will be impossible to avoid B-B and N-N linkages in such a structure, and the resultant molecules would be expected to be unstable. Indeed, experiments performed earlier in this group with laser-vaporized boron nitride targets to form cluster beams revealed no indication of fullerene cage formation.

4.2 Cage-doped Fullerenes with Boron

The fact that carbon appears to be the only element capable of forming stable geodesic cage molecules does not necessarily mean that only pure carbon cages can be formed. It should be possible to substitute a heteroatom every once in a while into the carbon network without destabilizing the entire cage. This is particularly true since the fullerene cage is closed. Even though the heteroatom may not produce as energetically stable a cage as carbon, the barrier of removal of this heteroatom may be sufficiently high that the substituted cage will have high kinetic stability. This is the case with the various common p-type and n-type donor atoms deep in the bulk of semiconductor lattices like silicon, for example.

The apparatus used for the generation of boron doped fullerenes is the FT-ICR spectrometer described in Chapter Three. Clusters are produced by laser vaporization of a graphite/boron nitride composite disk, which is prepared by mixing 15 wt % powder (Fischer) with graphite powder (Poco Graphite Inc.), and pressed into tablet form using a custom made die. Vaporization is accomplished with 10-20 mJ of the Nd:YAG second harmonic focused to a 0.1-

cm-diameter spot on the target disk. The timing of the laser vaporization pulse is adjusted in synchrony with the onset of the supersonic helium pulse so that extensive residual ionization from the laser plasma remained. The cluster ions studied here, both positive and negative, are the residual ions thus obtained.

Figure 23a shows a FT-ICR mass spectrum of a section of the positive cluster ions produced by laser vaporization of the BN-loaded graphite target disk. Although the detailed fine structure of the cluster ion peaks in this figure may be difficult to discern, it is clear that only even-numbered clusters are present just like in the case of pure carbon fullerenes shown in Figure 23b. More careful examination reveals that there is more fine structure to each of the major clumps than can be explained by carbon alone. Figure 24 shows in detail the fine structure near the 60 atom clump. Figure 24b displays pure C_{60} peaks at 720, 721, and 722 amu due to $^{12}C_{60}$, $^{12}C_{59}^{13}C$, and $^{12}C_{58}^{13}C_2$, respectively. In Figure 24a there are clearly cluster ions present in significant abundance at 719, 718, 717, 716, and 715 amu in addition to the 720, 721, 722 amu peaks. These are due to carbon clusters which have been doped with up to four boron atoms, i.e., $C_{59}B$, $C_{58}B_2$, $C_{57}B_3$ and $C_{56}B_4$.

Exact measurement of the relative importance of these various species in the ICR trap is complicated by the high natural abundance of the two stable isotopes of boron (20% ^{10}B , 80% ^{11}B). However, as demonstrated in earlier work from this group in studies of gallium arsenide clusters [70], it is possible to deconvolute the observed mass spectrum to obtain approximate relative compositions. The resulting compositions are found to vary somewhat shot-to-

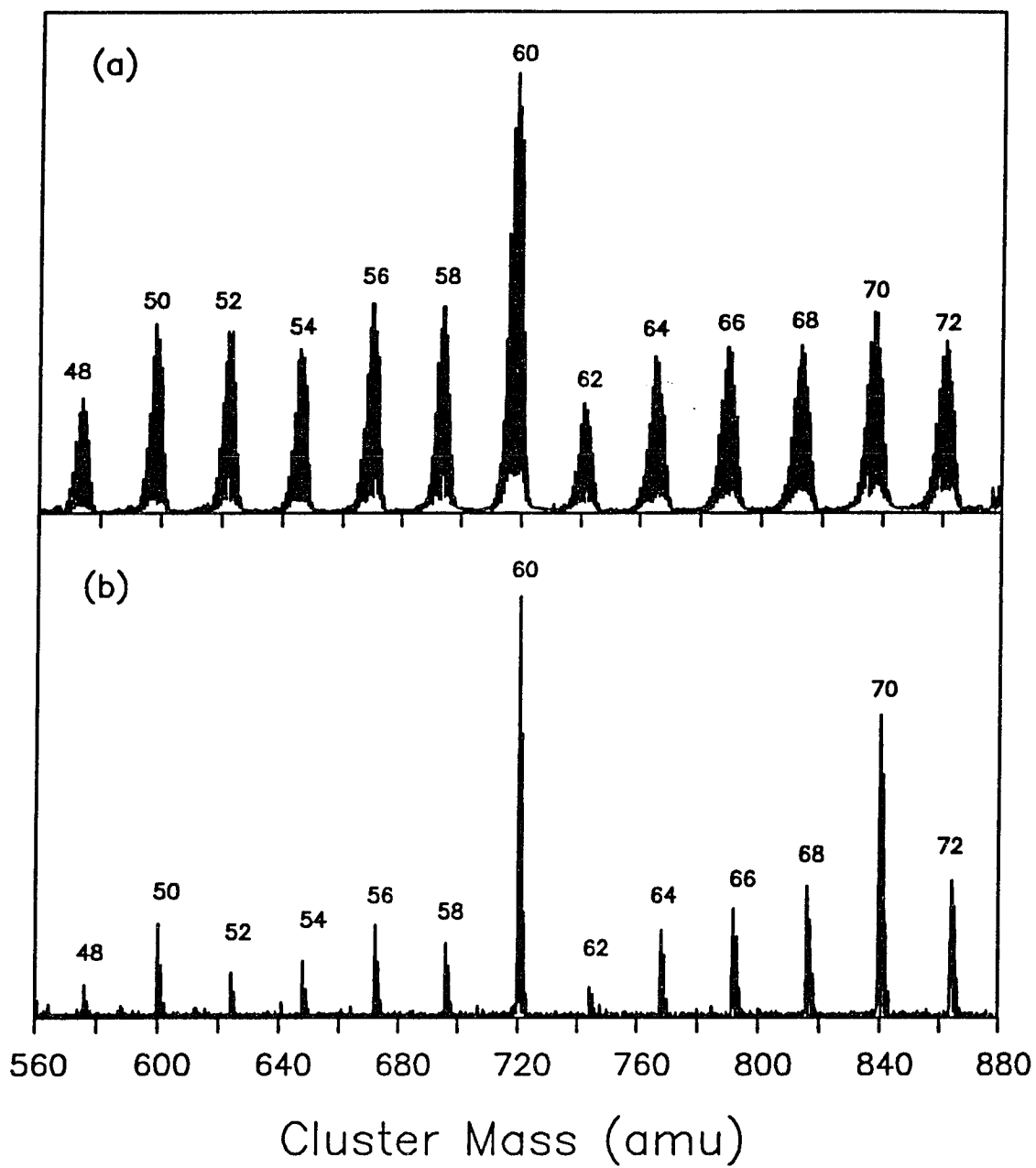


Figure 23. FT-ICR mass spectra of cluster cations prepared by laser vaporization of a (a) boron nitride/graphite composite disk (b) pure graphite disk in a supersonic nozzle.

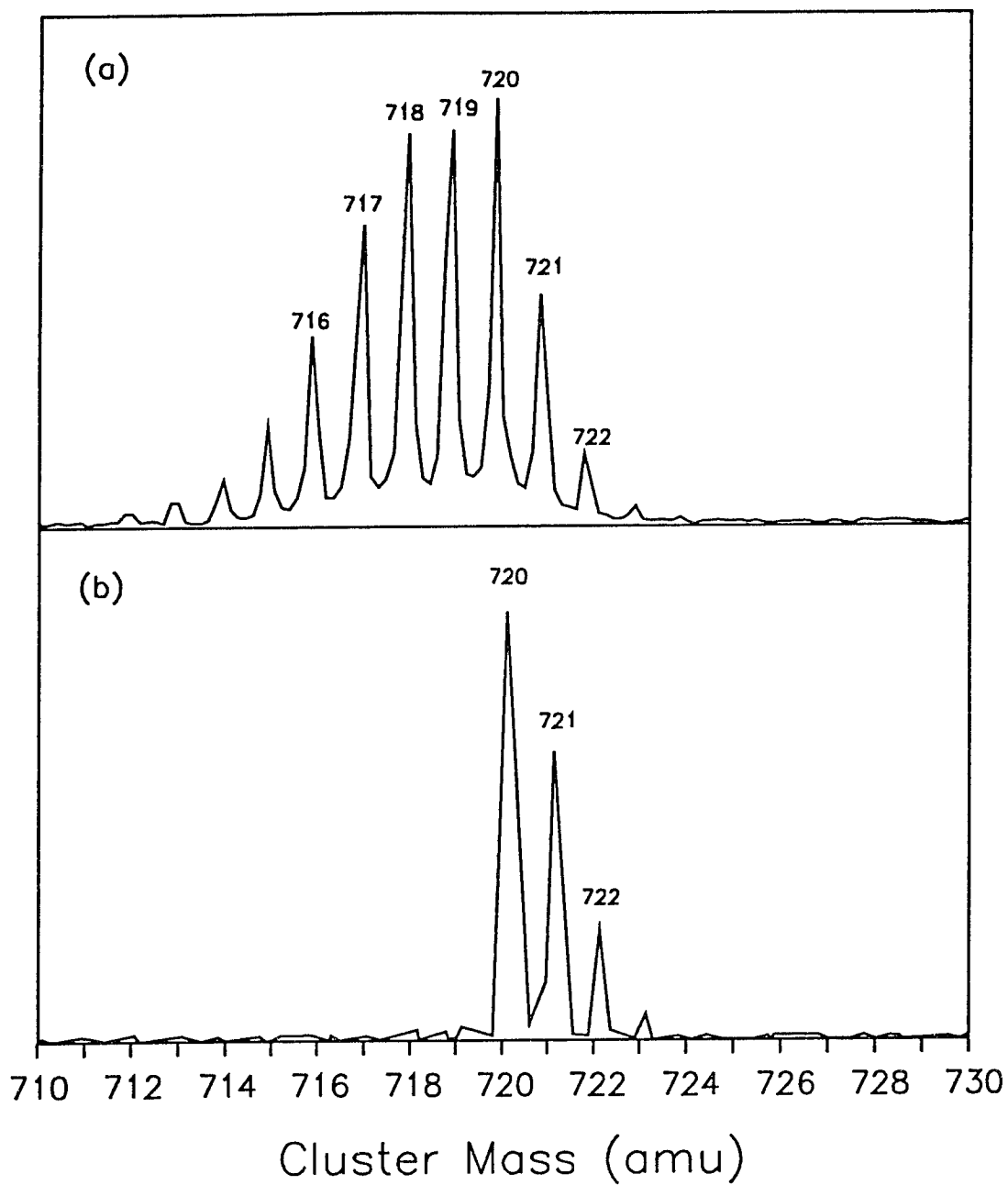


Figure 24. Expanded view of the mass spectra of 60 atom cluster cations. (a) boron nitride/graphite target disk; (b) pure graphite target disk. The mass peaks less than 720 amu in (a) reveals that boron has been substituted into the fullerenes.

shot. The mass spectrum shown in Fig. 24a is quite typical. In this case the approximate compositions are found to be 22% C₆₀, 21% C₅₉B, 24% C₅₈B₂, 18% C₅₇B₃, and 9% C₅₆B₄, with small amounts more extensively doped fullerenes. No evidence for significant nitrogen incorporation is found, although mass degeneracy with the pure carbon and boron-doped fullerenes prevent an accurate measure.

Essentially the same cluster distribution is obtained when graphite targets are impregnated with pure boron powder. We suspect the failure to produce nitrogen-doped clusters from the boron-nitride containing graphite targets is the facile formation of N₂ or (CN)₂ in the laser plasma. For this study, however, we will concentrate here on the boron doped features since these appear to be made in abundance, and are quite unambiguously identifiable in the mass spectrum.

The most important aspect of Figure 23a is that only even-numbered clusters are observed. As mentioned in last section, this is a single feature of carbon cluster distributions for which the only compelling explanation yet offered is that they are, in fact, fullerenes ---- *i.e.* closed geodesic spheres consisting of 12 pentagons and an appropriate number of hexagons. The fact that they each appear here with roughly the same amount of boron substitution strongly supports the notion that the boron atoms have been "doped" into the fullerene cages. Notice that the boron-doped cages still appear to be particularly stable with 50 and 60 atoms, just as with the corresponding pure carbon fullerenes.

Similar cluster mass spectra taken in higher mass ranges reveal, as expected, that the boron-doped 70 atom clusters are also particularly abundant.

The positive cluster distribution from this boron-nitride/graphite composite target is checked out to over 200 atoms. Throughout the 44-200 atom size range only the even-numbered clusters are evident. The extent of boron doping appears to increase roughly linearly with the cluster size, supporting the notion that boron incorporation into the growing carbon network under these source conditions is basically a statistical process.

Another indication that the boron atoms have been doped into the carbon network of the fullerene cage is their surface chemistry. Any such surface boron atoms should be connected to three carbon atoms in the cage through single covalent bonds. Particularly in this case of the positive ions, there is no question that these boron atoms should act as strong Lewis acid sites. Figure 25 shows the result of a test of this prediction by exposure of the mass-selected 60 atom clusters to NH_3 at a pressure of 1×10^{-6} torr for 2 seconds. Now it is quite clear that the boron-doped 60 atom (acidic) clusters have been rather effectively titrated by this ammonia base. Deconvolution of the isotopic fine structure on the observed ammoniated product peaks show them to be dominated by the single compositions labeled in Fig. 25b. As is evident in this figure, the borons in the doped buckminsterfullerene cage appear to be acting independently. Judging from the size of the NH_3 molecule, these boron atoms must be well separated from each other on the surface of the cage.

One of the most vivid demonstrations of the stability of fullerene cages has been their photofragmentation behavior. The lowest fragmentation channel for all fullerenes larger than C_{32} has been found to be C_2 loss [71, 72]. Since C_2 is quite weakly bound compared to C_3 and larger carbon radicals, the

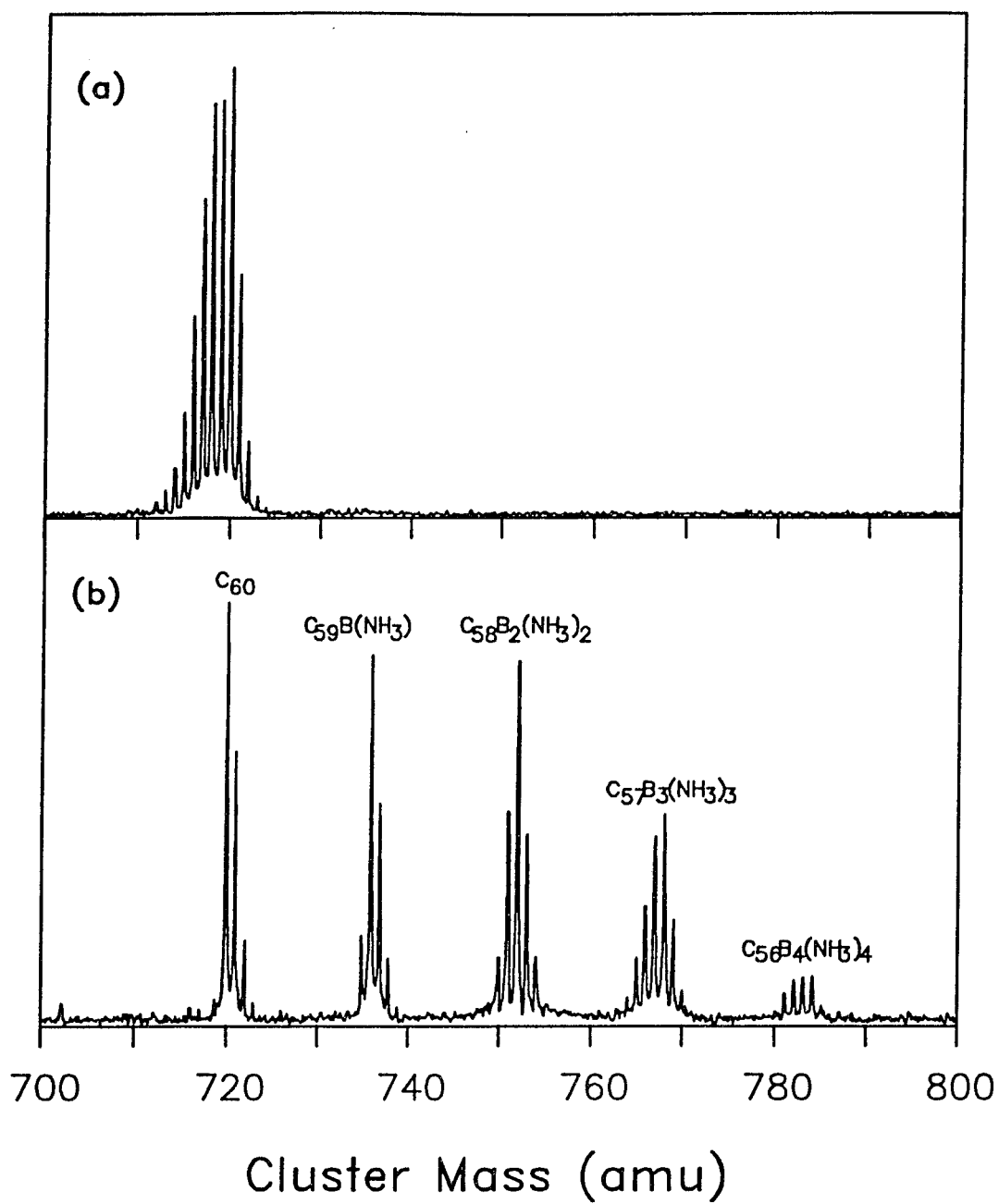


Figure 25. (a) FT-ICR mass spectrum of the 60 atom clusters produced as in Figure 22. All other clusters are selectively ejected from the ICR trap. (b) The result of exposure of the selected clusters to ammonia.

dominance of this fragmentation channel must be due to the stability of the other part of the molecule left behind. With this thought in mind a mechanism has been proposed [71] which involves the migration of the pentagons on the surface of the fullerene cage until two pentagons share an edge. The C_2 fragment can then leave in a concerted process which simultaneously forms the next smaller fullerene. This is the "shrink-wrapping" mechanism that was used several years ago to prove that metal atoms had been captured in the fullerene cage [71]. In the case of C_{60} , a recent estimate [72a] of the amount of internal energy required for this process to proceed at a rate that competes well with cooling by infrared emission, is over 30 eV. The photofragmentation behavior of boron-doped fullerene is therefore quite a stringent test of the ability of the boron to stay doped in the cage.

Figure 26 shows the result of a typical laser photolysis experiment. Here the positively charged clusters are prepared, as above, by laser vaporization of a boron nitride / graphite composite, and the clusters with 60 atoms are selected. The top panel shows the FT-ICR mass spectrum of the 60 atom cluster prior to irradiation, the bottom shows the resultant spectrum after 2 second exposure to XeCl excimer laser pulses at a repetition rate of 50 s^{-1} , and an average fluence of 90 mJ cm^{-2} per pulse. Note that only even-numbered photofragments are observed, and that the mass spectrum clearly shows that these fragments still contain boron.

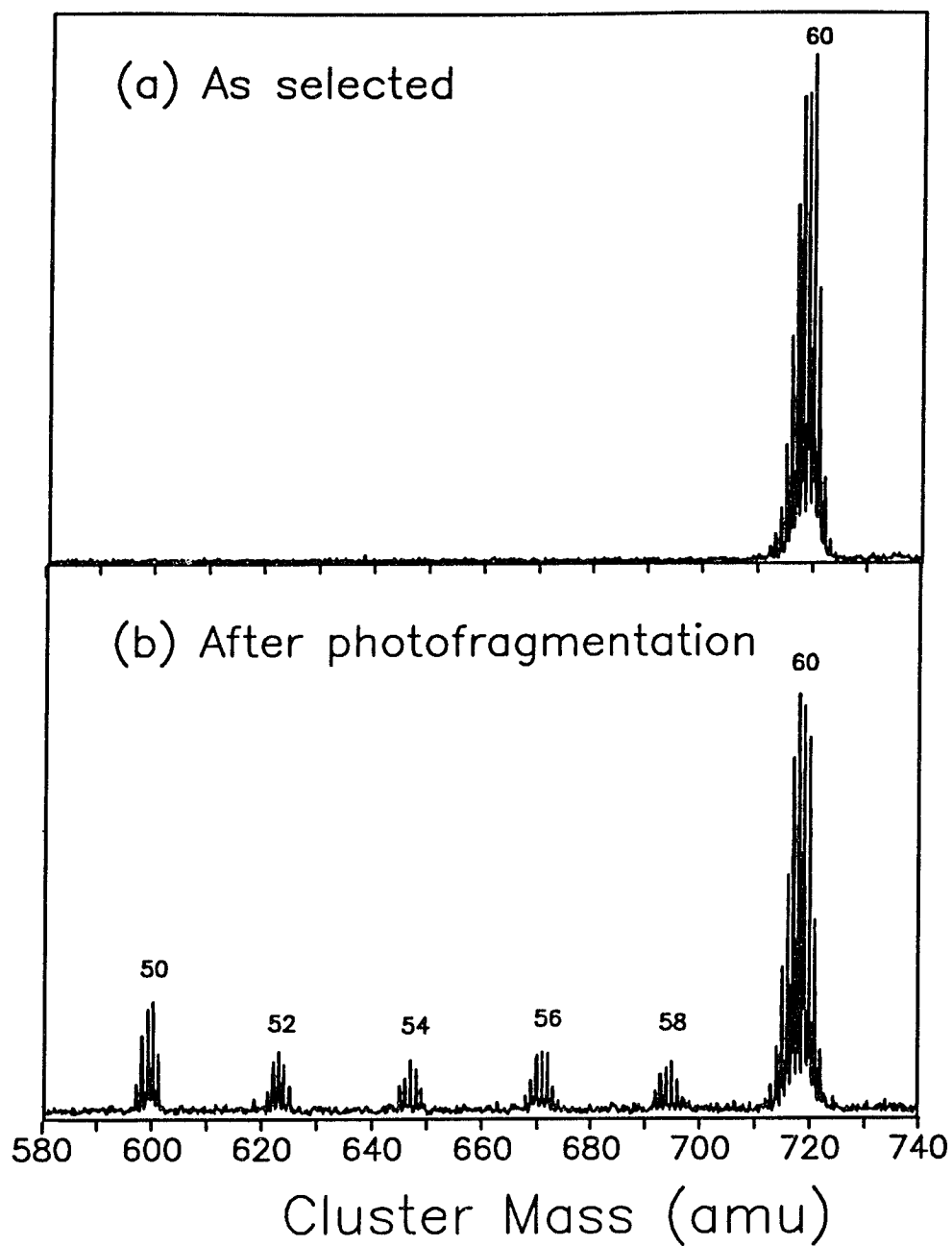


Figure 26. FT-ICR mass spectra showing result of photolysis of the levitated 60-atom clusters. Top panel (a) shows the originally selected clusters prior to irradiation. Bottom panel (b) reveals the formation of daughter fragments by successive loss of a dimer.

Similar photolysis experiments are performed with a range of laser pulse energies and dosage times. As with pure C_{60} , the boron-doped 60-fullerenes are found to fragment by loss of C_2 and other even-numbered units to produce successively smaller fullerenes, this "shrinking" process breaking off abruptly at the 32-fullerene. Detailed study of the cluster mass distribution shows the level of boron doping in the fragments decreased somewhat as the shrinking process continued. For example, by the time the fullerene had decreased in size to 50 atoms, a typical measured composition is 28% C_{50} , 43% $C_{49}B$, 18% $C_{48}B_2$, 12% $C_{47}B_3$.

Andreoni *et al.* [73] investigated theoretically the properties of $C_{59}B$ and found that doping induces important changes in both ionic and electronic behaviors of C_{60} . The HOMO is strongly localized and can act like an electron acceptor state just as in the case of deep impurity states in semiconductors. These cage-doped fullerenes may open new pathways to the synthesis of new materials with interesting properties.

4.3 Metallofullerenes

As an evidence for the then controversial caged structure proposal of C_{60} , Smalley and coworkers reported that a single lanthanum atom could be trapped inside by laser vaporization of a graphite target impregnated with $LaCl_3$ [74]. Attempting to make cage doped fullerenes with metal inside, we laser vaporize a 10 wt % LaB_6 / graphite powder mixture disk in the FT-ICR apparatus much the same way as we did to generate B-doped fullerenes. The FT-ICR mass spectrum shows that both empty fullerenes and fullerenes with metal atom

inside are produced in the cluster source. Figure 27 shows a detailed view in the 860 amu mass range. Let's ignore the boron isotope distribution for the moment, the mass spectrum can be explained in the following way: first C_{60} with lanthanum inside the cage, $La@C_{60}$, has been made, and they are the peaks at 859 amu, 860 amu, and 861 amu. The peaks at 858 amu, 857 amu, and 856 amu which are 1, 2, and 3 amu less than the 859 amu $La@C^{12}_{60}$ peak are due to the doping of the $La@C_{60}$ cage with one, two, and three boron atoms respectively. In another words, $La@C_{59}B$, $La@C_{58}B_2$, and $La@C_{57}B_3$ have been made in the process.

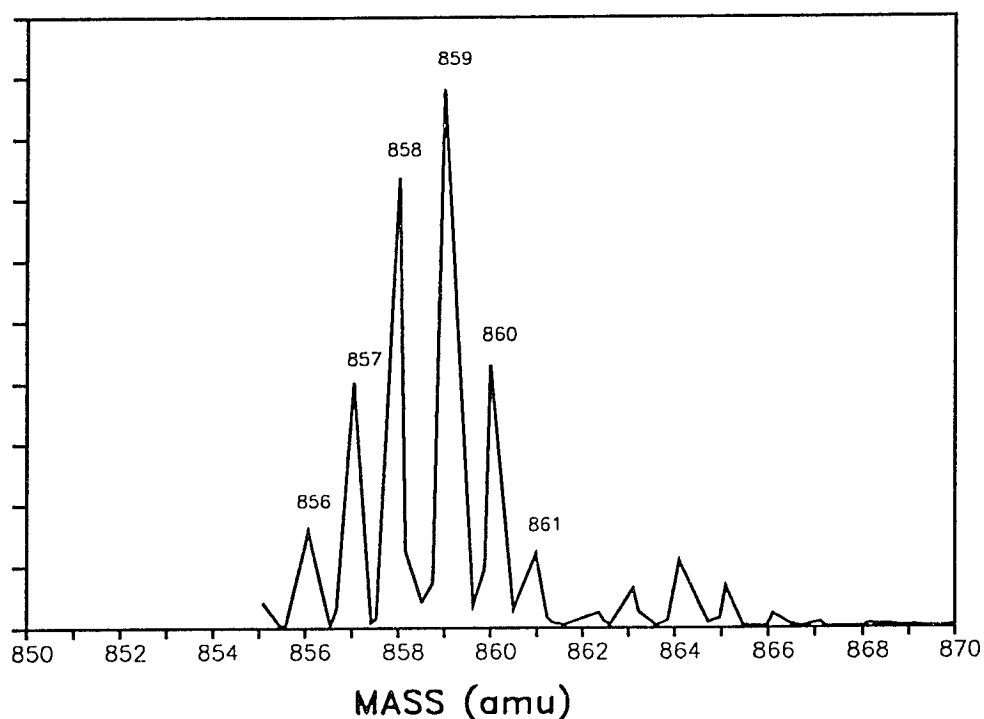


Figure 27. Expanded view around 860 amu range of the FT-ICR mass spectrum produced using a LaB_6 /graphite composite target disk.

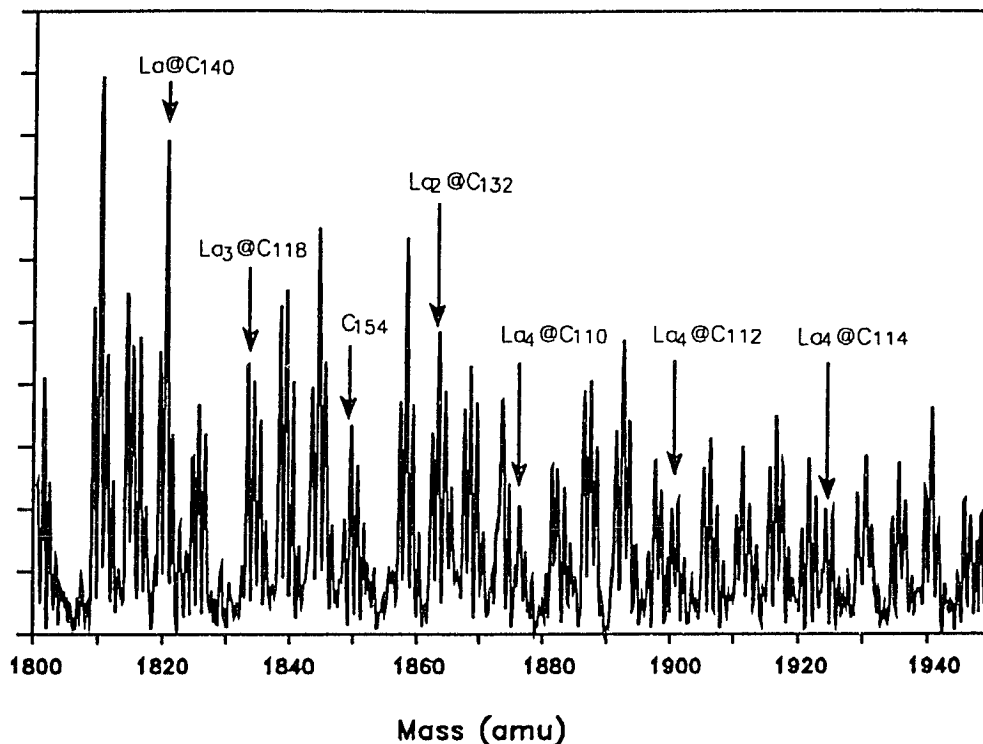


Figure 28. FT-ICR mass spectrum showing the existence of fullerenes with up to four lanthanum atoms trapped inside.

We have prepared cage doped fullerenes with several carbon atoms replaced by several boron atoms, but so far there is only a single metal atom trapped inside the fullerenes. In the course of studying the metallofullerenes produced in the supersonic beams by means of laser vaporization in the FT-ICR apparatus, we find a very interesting result concerned with the time development of the mass spectrum using a 10% La_2O_3 / graphite mixture target disk. On the initial pass of the laser light though the fresh surface, the cluster distribution is dominated by empty fullerenes C_n , with some signal intensity of La@C_n

lanthanum fullerenes evident. On the second pass of the previous laser treated region of the disk, the mass spectrum changes, and the La@C_n become most abundant and some clusters with mass peaks corresponding to La_2C_n appear on the spectrum. Further laser blasting of the same regions continue to change the mass distribution, showing strong signal for La_3C_n and even La_4C_n . Figure 28 shows the 1800-1950 amu region of this cluster distribution after further laser "aging" of the target composite disk. Now clusters with 4 lanthanum atoms are evident as well.

As we did in the case of B-doped fullerenes, a series of chemical reactions with O_2 and ammonia and XeCl excimer laser photofragmentation test are performed on these lanthanum fullerenes to check if the metal atoms are inside or outside the cage. If they were outside the cage, the lanthanum atoms should readily react with O_2 , and be dissociated first from the compounds upon enough laser irradiation. Yet, as levitated positive ions in the ICR cell, they are chemically inert, and they fragment only by successive C_2 loss, proving that all lanthanum atoms are trapped inside the fullerene cage to form endohedral metallofullerenes--- $\text{La}_2\text{@C}_n$, $\text{La}_3\text{@C}_n$, and $\text{La}_4\text{@C}_n$.

The fact that fullerenes with multi-metal atoms inside grow in intensity upon laser aging of the disk indicates that later laser shots on the disk are probing consequent materials produced in previous laser shot. The initial laser blast probably causes La@C_n - La@C_n coalescence reactions occurring either on the surface or in the laser-induced plasma just above the surface.

The smallest cage that can surround one lanthanum atom is found to be C_{44} , for two lanthanum atoms it is C_{66} , and the minimum cage that can fit

around three is C_{88} , while for four lanthanum atoms it is C_{110} . The difference is a constant 22 carbon atoms. This may be due to the formation of these clusters by metallofullerene coalescence reactions which lead to tubular metallofullerene "nanowires" filled with a line of metal atoms arranged much like peas in a pod. If we assume the spiral structure, 22 is the exact number of carbon atoms needed to make one turn of the tube. Perhaps these nanowires are yet another generation of descendants of the fullerene family.

In order to utilize most of the scientific research tools to study these metallofullerenes and to explore future technical applications, macroscopic quantities of endohedral fullerene complexes have to be made. Our initial success in this area is the "mass production" of fullerenes with a single lanthanum atoms trapped inside the carbon cage by means of laser vaporization of a lanthanum oxide / graphite composite rod in a flow of argon at 1200 °C in a oven [75]. The detailed description of the apparatus has been given elsewhere [10]. The materials are sublimed onto a ICR copper disk substrate forming a mirrorlike black film.

The film is analyzed by laser desorption mass spectrometry (LDMS) using the FT-ICR apparatus. The vaporization laser is kept at low fluence (below 1.0 mJ in a 0.1-cm-diameter spot on the sample disk) so that fullerenes can be desorbed with no or little fragmentation and mostly as neutrals. Ionization is accomplished by a ArF excimer laser crossing the neutral cluster beam just before it enters the ICR cell. The resulting mass spectrum is shown in Figure 29. $La@C_{60}$, $La@C_{70}$, $La@C_{74}$, and $La@C_{82}$ are prominent in the spectrum, indicating the existence metallofullerenes in these macroscopic sized films.

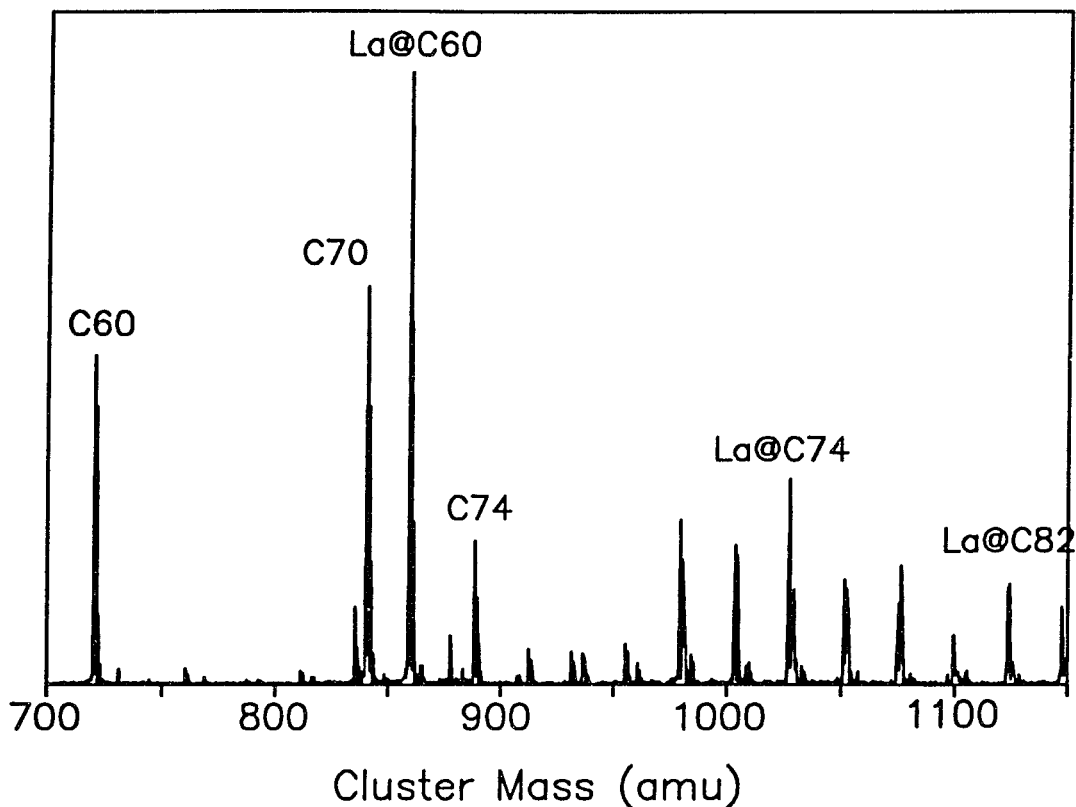


Figure 29. FT-ICR LDMS analysis of the sublimed fullerene film showing presence of La@C_n .

We further Soxhlet extract the sublimed materials in boiling toluene for 2 hours. The resultant solution is evaporated to almost total dryness and deposited onto the ICR copper disk substrate and analyzed in the same gentle way in the FT-ICR apparatus. Figure 30 shows the resulting mass spectrum. The only lanthanum-containing fullerene to be extracted by hot toluene is found to be La@C_{82} .

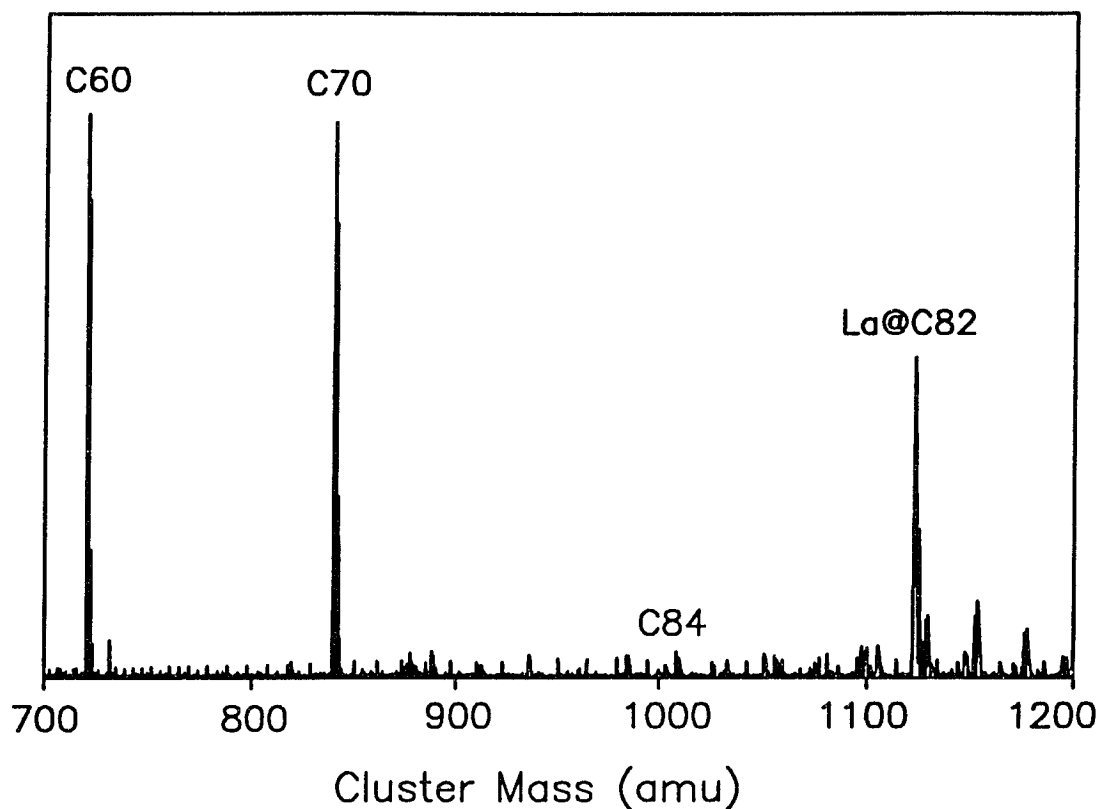


Figure 30. FT-ICR mass spectrum of hot toluene extract of fullerene materials produced by laser vaporization.

Similar results are also obtained with endohedral yttrium-fullerenes. $Y@C_{60}$, $Y@C_{70}$, $Y@C_{74}$, and $Y@C_{82}$ are abundant in the sublimed films, and for the first time a multimetal endohedral complex fullerene $Y_2@C_{82}$ is found not only abundant in the sublimed films but also soluble in hot toluene.

Chapter Five

Conclusion and Outlook

The ultraviolet photoelectron spectra of semiconductor Ga_xAs_y cluster anions show that the electrons of these small clusters are all paired up just like in the cases of bulk surfaces. Because the extra electron on the surface is localized, it does not take a very large sized cluster to mimic the surface effect in term of electron affinity, and from the fact that there are certain phenomena common to both small semiconductor clusters and bulk surfaces, these small clusters may indeed serve as models for the later. It is desirable to extend the electron affinity measurement to other semiconductor clusters such as InP to see whether the EA oscillation still exists and how fast the EA approaches the bulk value.

The results on shell closing in metal cluster plus adsorbate systems reveal the intimate relationship between theory and experiment in the field of cluster science, one of the major argument for the "cluster model" of real bulk surfaces. Here the jellium model developed for metal bulk surfaces is applied to the case of metal clusters. The experiment is performed on various sized metal clusters under UHV condition in gas phase, and the results agree very well with the high level theoretical calculation. This agreement has important impact on the theoretical picture, i.e. bond preparation, for chemisorption on bulk surfaces implemented in the theoretical calculations, and these theoretical models

checked by our cluster experiments will no doubt shine light in the experimental field of bulk surface sciences. What a wonderful interplay.

Common grounds between clusters and bulk surfaces are often found in other systems also. For example, image charge states caused by an electron just outside a metal surface have been discovered and studied by surface scientists [76, 77]. The question remains whether equivalent phenomenon occurs on metal clusters so that we can use the small clusters to model the bulk surfaces. We have obtained high resolution vibrational autodetachment spectra of Au_6^- using the UPS apparatus [78], where we used a dye laser as the detachment laser and scanned the photon wavelength near the detachment threshold. It was found that even for such a 6 atom metal cluster anion there indeed exist image charge bound states much like in the case of bulk surfaces. Furthermore a D_{6h} ring structure was proposed for Au_6^- based on the spectral results. In the case of alkali halide clusters, the bounding of the excess electrons in KI cluster anions have been explored by photoelectron spectroscopy and photofragmentation as a joint project between our group at Rice University and Bloomfield group at University of Virginia [79]. The results showed that small KI clusters is just like small pieces of bulk in many aspects ---- they take the KI bulk lattice structure in most cases, and there exist color centers on some clusters, therefore many bulk solid and surface properties can be learned from these clusters.

On the practical application side, the discovery of C_{60} probably is the most important event for the purpose of using clusters as novel materials. Because of the explosive expansion in the areas of research and applications of these materials, fullerenes themselves have formed their own field, but still they

are initially discovered and studied in the gas phase studies of clusters. Currently the most technologically interesting properties of bulk C_{60} are electronic. Boron doped fullerenes may well be used in semiconductor devices in the future, and fullerenes with different elements trapped inside will no doubt exhibit unusual properties different from the elements that trapped in and the fullerenes themselves, and a whole new class of carbon caged materials may appear as a result. If the proposed tabular metallofullerene structure is correct, these nanowires could be used to extend the much interested microelectronic technology to even finer levels ---- connecting logic and memory block with single lines of atoms.

However, any practical use can only come after the mass production and isolation of these doped fullerenes. Although boron doped fullerenes can be made easily in the gas phase, no success has been reported on the mass production. This difficulty could be because the boron site of the cage is quite reactive, and the boron doped fullerenes are polymerized with others and destroyed themselves after being made. One could try to solve this problem in the future by titrating them with ammonia before they contact with other molecules and then extracting them out. The lack of nitrogen doped fullerenes even in the gas phase is believed to be due to kinetic reasons rather than instability. Solutions need to be found so that in the synthetic process nitrogen can be incorporated onto the cage before forming a more stable molecule and getting away. At the moment of writing this thesis, world wide effort has been concentrating on the separation and isolation of metal doped fullerenes. It is believed that the time that these exotic molecules are used to serve the mankind will be coming soon.

References

1. *Physics and Chemistry of Small Clusters*, edited by P. Jena, B. K. Rao, and S. N. Khanna (1987).
2. a) E.L. Muetterties, *Bull. Soc. Chem. Belg.* **84**, 959 (1975).
b) E. Shustorovich, R. C. Baetzold, and E. L. Muetterties, *J. Phys. Chem.* **87**, 1100 (1983).
3. a) R. E. Smalley, in *Comparison of Ab Initio Quantum Chemistry with Experiment for Small Molecules State-of-the-Art*, edited by R. J. Bartlett, 53 (1985).
b) R. E. Smalley, in *Metal-Metal Bonds and Clusters in Chemistry and Catalysis*, edited by J. P. Fackler, 249 (1989)
4. R. P. Andres, R. S. Averback, W. L. Brown, L. E. Brus, W. A. Goddard, A. Kaldor, S. G. Louie, M. Moscovits, P.S. Peercy, S. J. Riley, R. W. Siegel, F. Spaepen, and Y. Wang, *J. Mater. Res.* **4**, 704 (1989).
5. a) T. G. Dietz, M.A. Duncan, D. E. Powers, and R. E. Smalley, *J. Chem. Phys.* **74**, 6511 (1981).
b) R. E. Smalley, in *Laser as Reactant and Probes in Chemistry*, edited by W. M. Jackson and A. B. Harvey (1985).
c) D. E. Powers, S. G. Hanson, M. E. Geusic, A. C. Puiu, J. B. Hopkins, T. G. Dietz, M. A. Duncan, P. R. R. Langridge-Smith, and R. E. Smalley, *J. Phys. Chem.* **86**, 2556 (1982).
6. S. J. Riley, E. K. Parks, C. R. Mao, L.G. Pobo, and S. Wexler, *J. Phys. Chem.* **86**, 3911 (1982).
7. V. E. Bondybey and J. H. English, *J. Chem. Phys.* **80**, 568 (1984).

8. H. W. Kroto, J. R. Heath, S. C. O'brien, R. F. Curl, and R. E. Smalley, *Nature* **318**, 165 (1985).
9. W. Kratschmer, L. D. Lamb, K. Fostiropoulos, D. R. Huffman, *Nature* **347**, 354 (1990).
10. R. E. Haufler, Y. Chai, L. P. F. Chibante, J. Conceicao, Changming Jin, Lai-Sheng Wang, Shigeo Maruyama, R. E. Smalley, *Mater. Res. Soc. Symp. Proc.* **206**, 627 (1990).
11. *Fullerenes --- Synthesis, Properties and Chemistry of Large Carbon CLusters*, edited by G. S. Hammond and V. J. Kuck, ACS Symposium Series (1991).
12. J. S. Blakemore, *J. Appl. Phys.* **53**, R123 (1982), and references therein.
13. J. S. Blakemore in *Gallium Arsenide*, edited by J. S. Blakemore, 3 (1987).
14. R. J. Meyer, C. B. Duke, A. Paton, A. Kahn, E. So, J. L. Yeh, and P. Mark, *Phys. Rev. B* **19**, 5194 (1979).
15. X. Zhu, S.B. Zhang, S.G. Louie and M.L. Cohen, *Phys. Rev. Lett.* **63**, 2112 (1989).
16. J. van Laar, A. Huijser and T. L. van Rooy, *J. Vac. Sci. Technol.* **14**, 894 (1977).
17. W. R. Gentry in *Atomic and Molecular Beam Methods*, Vol.1, edited by G. Scoles, 64 (1988).
18. S. C. O'Brien, Y. Liu, Q. Zhang, J. R. Heath, F. K. Tittel, R. F. Curl, and R. E. Smalley, *J. Chem. Phys.* **84**, 4074 (1986).

19. Y. Liu, Q. L. Zhang, F. K. Tittle, R. F. Curl, and R. E. Smalley, *J. Chem. Phys.* **85**, 7434 (1986).
20. O. Cheshovsky, S.H. Yang, C. L. Pettiette, M. J. Craycraft, and R. E. Smalley, *Rev. Sci. Inst.* **58**, 2131 (1987).
21. M. G. Liveman, S. M. Beck, D. L. Monts, and R. E. Smalley, *Rarefied Gas Dynam.* **11**, 192 (1979).
22. Josie Conceicao, M. A. Thesis, Rice University (1991).
23. K. J. Taylor, Ph.D. Thesis, Rice University (1990).
24. W. C. Wiley and I. H. McLaren, *Rev. Sci. Inst.* **26**, 1150 (1955).
25. C. W. S. Conover, Y. J. Twu, Y. A. Yang, and L. A. Bloomfield, *Rev. Sci. Inst.* **60**, 1065 (1989).
26. H. Hotop and W. C. Lineberger, *J. Chem. Phys.* **58**, 2379 (1979).
27. C. E. Moore, *Atomic Energy Levels* vol. III (1971).
28. L. Lou, L. Wang, L. P. F. Chibante, R. T. Laaksonen, P. Nordlander, R. E. Smalley, *J. Chem. Phys.* **94**, 8015 (1991).
29. G. W. Lemire, G. A. Bishea, S. A. Heidecke, and M. D. Morse, *J. Chem. Phys.* **92**, 121 (1990).
30. a) K. Balasubramanian, *J. Chem. Phys.* **86**, 3410 (1987).
b) K. Balasubramanian, *J. Mol. Spectroscopy* **139**, 405 (1990).
31. G. Scuseria, Private Communication.

32. M. M. Kappes, M. Schar, U. Rothlisberger, C. Yeretizian, and E. Schumacher, Chem. Phys. Lett. **143**, 251 (1988).
33. W. Saunders, K. Clemenger, W. de Heer and W. Knight, Phys. Rev. B **32**, 1366 (1985).
34. O. Cheshnovsky, K. J. Taylor, J. Conceicao, and R.E. Smalley, Phys. Rev. Lett. **64**, 1785 (1990).
35. K. J. Taylor, C. L. Pettiette, O. Cheshnovsky, and R. E. Smalley, J. Chem. Phys., in press (1992).
36. L. E. Brus, J. Chem. Phys. **84**, 4074 (1983).
37. M. A. Olshavsky, A. N. Goldstein, A. P. Alivisatos, J. Am. Chem. Soc. **112**, 9438 (1990).
38. M. Gratzel, Nature **349**, 740 (1991).
39. a) K. D. Kolenbrander and M. L. Mandich, Phys. Rev. Lett. **65**, 2169 (1990).
b) K. D. Kolenbrander and M. L. Mandich, J. Chem. Phys. **92**, 4759 (1990).
40. A. Zangwill, *Physics at Surfaces* (1988).
41. W. D. Knight, K. Clemenger, W. A. de Heer, W. A. Saunders, M. Chou, and M. L. Cohen, Phys. Rev. Lett. **52**, 2141 (1984).
42. K. Clemenger, Phys. Rev. B **86**, 619 (1986).
43. W. A. Saunders, Ph.D. thesis, Berkeley (1986).
44. S. G. Nilsson and K. D. Vidensk, Selsk. Mat. Fys. Medd. **29**, No. 16 (1955).

45. C. L. Pettiette, S. H. Yang, M. J. Craycraft, J. Conceicao, R. T. Laaksonen, O. Cheshnovsky, and R. E. Smalley, *J. Chem. Phys.* **88**, 5377 (1988).
46. G. Blyholder, *J. Phys. Chem.* **68**, 2772 (1964).
47. M. W. Roberts, *Chem. Soc. Rev.* **6**, 373 (1977).
48. P. S. Bagus, K. Hermann, C. W. Bauschlicher and B. Bunsenges, *Phys. Chem.* **88**, 302 (1984).
49. a) I. Panas, J. Schule, P. Siegbahn and U. Wahlgren, *Chem. Phys. Lett.* **149**, 265 (1988).
b) J. Schule, P. Siegbahn and U. Wahlgren, *J. Chem. Phys.* **89**, 6982 (1988).
c) P.E. M. Siegbahn, L. G. M. Pettersson and U. Wahlgren, *J. Chem. Phys.* **94**, 4024 (1991).
d) P.E. M. Siegbahn and U. Wahlgren, *Intern. J. Quantum Chem.* in press.
50. M. A. Nygren, P. E. M. Siegbahn, C. Jin, T. Guo, and R. E. Smalley, *J. Chem. Phys.* **95**, 6181 (1991).
51. D.P. Chong and S.R. Langhoff, *J. Chem. Phys.* **84**, 5606 (1986).
52. R.E. Leuchtner, A.C. Harms and A.W. Castleman, Jr, *J. Chem. Phys.* **92**, 6527 (1990).
53. a) R. E. Leuchtner, A. C. Harms, and A. W. Castleman, Jr., *J. Chem. Phys.* **91**, 2753 (1989);
b) R. E. Leuchtner, A. C. Harms, and A. W. Castleman, *J. Chem. Phys.* **94**, 1093 (1991).

- 54. S. Maruyama, L. R. Anderson, and R. E. Smalley, *Rev. Sci. Instrum.* **61**, 3686 (1990).
- 55. J. M. Alford, R. T. Laaksonen, and R. E. Smalley, *J. Chem. Phys.* **94**, 2618 (1991).
- 56. A. G. Marshall, T. C. L. Wang, and T. L. Ricca, *J. Am. Chem. Soc.* **107**, 7893 (1985).
- 57. A. G. Marshall and F. R. Verdun, *Fourier Transforms in NMR, Optical, and Mass-Spectrometry* (1990).
- 58. a) R. B. Cody, R. C. Burnier and B. S. Freiser, *Anal. Chem.* **54**, 96 (1982).
b) R. C. Burnier, R. B. Cody and B. S. Freiser, *J. Am. Chem. Soc.* **104**, 7436 (1982).
- 59. C. E. C. A. Hop, T. B. McMahon and G. D. Willett, *Int. J. Mass Spect. Ion Proc.* **101**, 191 (1990).
- 60. Lihong Wang, Ph.D. thesis, Rice University (1992).
- 61. G. Gioumousis and D. P. Stevenson, *J. Chem. Phys.* **29**, 294 (1958).
- 62. a) J. Harris and S. Anderson, *Phys. Rev. Lett.* **55**, 1583 (1985).
b) J. Harris, S. Anderson, C. Holmberg, and P. Nordlander, *Physica Scripta T* **13**, 155 (1986).
- 63. M. D. Morse, M. E. Geusic, J. R. Heath, and R. E. Smalley, *J. Chem. Phys.* **83**, 2293 (1985).
- 64. Q. L. Zhang, S. C. O'Brien, J. R. Heath, Y. Liu, R. F. Curl, H. W. Kroto, and R. E. Smalley, *J. Phys. Chem.* **90**, 525 (1986).

65. R. L. Whetten, M. M. Alvarez, S. J. Anz, K. E. Schriver, R. D. Beck, F. N. Diederich, Y. Rubin, R. Ettl, C. S. Foote, A. P. Darmany, J. W. Arbogast, *Mat. Res. Soc. Symp. Proc.* **206**, (1990).
66. R. E. Haufler, J. Conceicao, L. P. F. Chibante, Y. Chai, N. E. Byrne, S. Flanagan, M. M. Haley, S. C. O'Brien, C. Pan, Z. Xiao, W. E. Billups, M. A. Ciufolini, R. H. Hauge, J. L. Margrave, L. J. Wilson, R. F. Curl, and R. E. Smalley, *J. Phys. Chem.* **94**, 8634 (1990).
67. J. H. Holloway, E. G. Hope, R. Taylor, G. J. Langley, A. G. Avent, T. J. Dennis, J. P. Hare, H. W. Kroto, and D. R. M. Walton, *Chem. Soc. Chem. Commun.* **14**, 966 (1991).
68. A. F. Hebard, M. J. Rosseinsky, R. C. Haddon, D. W. Murphy, S. H. Glarum, T. T. M. Palstra, A. P. Ramirez, and A. R. Kortan, *Nature* **350**, 600 (1991).
69. a) Curl, R. F; Smalley, R. E. *Science* **242**, 1017 (1988).
b) Smalley, R. E., "Supersonic Carbon Cluster Beams", in *Atomic and Molecular Clusters*, E. R. Bernstein, editor, Studies in Physical and Theoretical Chemistry, **68**, 1 (1990).
70. L. H. Wang, L. P. F. Chibante, F. K. Tittel, R. F. Curl, and R. E. Smalley, *Chem. Phys. Lett.* **172**, 335 (1990).
71. a) S. C. O'Brien, J. R. Heath, R. F. Curl, and R. E. Smalley, *J. Chem. Phys.* **88**, 220 (1988).
b) F. D. Weiss, S. C. O'Brien, J. L. Elkind, R. F. Curl, and R. E. Smalley, *J. Am. Chem. Soc.* **110**, 4464 (1988).
72. a) P. P. Radi, M-T Hsu, M. E. Rincon, P. R. Kemper, and M. T. Bowers, *Chem. Phys. Lett.* **174**, 223 (1990);
b) P. P. Radi, T. L. Bunn, P. R. Kemper, M. E. Molchan, and M. T. Bowers, *J. Chem. Phys.* **88**, 2809 (1988).

73. W. Andreoni, F. Gygi, and M. Parrinello, Chem. Phys. Lett. **190**, 159 (1992).
74. J. R. Heath, S. C. O'Brien, Q. Zhang, Y. Liu, R. F. Curl, H. W. Kroto, F. K. Tittel, R. E. Smalley, J. Am. Chem. Soc. **107**, 7779 (1985).
75. Y. Chai, T. Guo, C. Jin, R. E. Haufler, L. P. F. Chibante, J. Fure, L. Wang, J. M. Alford, and R. E. Smalley, J. Phys. Chem. **95**, 7564 (1991).
76. R. W. Schoenlein, J. G. Fujimoto, G. L. Eesley, and T. W. Capehart, Phys. Rev. Lett. **61**, 2596 (1988).
77. P. M. Echenique and J. B. Pendry, Progress in Surf. Sci. **32**, 111 (1989).
78. K. J. Taylor, C. Jin, J. Conceicao, L.-S. Wang, O. Cheshnovsky, B. R. Johnson, P. J. Nordlander, and R. E. Smalley, J. Chem. Phys. **93**, 7515 (1990).
79. Y.-A. Yang, L. Bloomfield, C. Jin, L.-S. Wang, K. J. Taylor, and R. E. Smalley, J. Chem. Phys. in press.